Materials Today • Volume xxx, Number xx • xxxx 2021

Selective area regrowth and doping for vertical gallium nitride power devices: Materials challenges and recent progress

Houqiang Fu [1,2,*,†], Kai Fu [1,†], Chen Yang [1], Hanxiao Liu [3], Kevin A. Hatch [3], Prudhvi Peri [4], Dinusha Herath Mudiyanselage [2], Bingjun Li [5], Tae-Hyeon Kim [6], Shanthan R. Alugubelli [3], Po-Yi Su [3], Daniel C. Messina [3], Xuguang Deng [1], Chi-Yin Cheng [1], Reza Vatan Meidanshahi [1], Xuanqi Huang [1], Hong Chen [1], Tsung-Han Yang [1], Jingan Zhou [1], Andrew M. Armstrong [7], Andrew A. Allerman [7], Edward T. Yu [6], Jung Han [5], Stephen M. Goodnick [1], David J. Smith [3], Robert J. Nemanich [3], Fernando A. Ponce [3], Yuji Zhao [1,*]

[1] School of Electrical, Computer, and Energy Engineering, Arizona State University, Tempe AZ, 85287 USA
[2] Department of Electrical and Computer Engineering, Iowa State University, Ames, IA 50011, USA
[3] Department of Physics, Arizona State University, Tempe, AZ 85287, USA
[4] School for Engineering of Matter, Transport and Energy, Arizona State University, Tempe, AZ 85287, USA
[5] Department of Electrical Engineering, Yale University, New Haven, CT 06511, USA
[6] Department of Electrical and Computer Engineering, The University of Texas at Austin, Austin, TX 78758, USA
[7] Sandia National Laboratories, Albuquerque, NM 87185, USA

This paper reviews materials challenges and recent progress for selective area regrowth and doping for vertical gallium nitride (GaN) power devices. The purpose is to realize randomly placed, reliable, contactable, and generally useable laterally patterned p-n junctions, which are the building blocks for various advanced power rectifiers and transistors. The general regrowth process and regrowth dynamics in trenches were discussed, where the effects of trench geometries, growth methods, and bulk substrates were elucidated. Comprehensive materials characterization techniques were utilized to analyze the regrown structures, including scanning electron microscopy, transmission electron microscopy, atom probe tomography, scanning probe microscopy, and secondary-ion mass spectrometry. Cathodoluminescence and secondary electrons in scanning electron microscopy and atom probe tomography were used to achieve lateral and vertical dopant profiling at a sub-micron scale. The regrowth interface after dry etching accumulated a high density of impurities and charges, contributing to the formation of a p^+-n^+ tunneling junction. This hypothesis was further confirmed by the electrostatic potential profile at the regrowth interface using electron holography. Novel etching technologies were investigated to improve the regrowth interface. It was found that low-power dry etching significantly reduced the interfacial charges and the reverse leakage currents of regrown p-n junctions. Photoelectrochemical wet etching was found to be effective in reducing deep-level defects near the regrowth interface. Atomic layer etching uses self-limiting chemical processes, thus removing

---

* Corresponding authors.
E-mail addresses: Fu, H. (houqiang@iastate.edu), Zhao, Y. (yuji.zhao@asu.edu).

† The two authors contributed equally to this work.

https://doi.org/10.1016/j.mattod.2021.04.011

Please cite this article in press as: H. Fu et al., Materials Today, (2021), https://doi.org/10.1016/j.mattod.2021.04.011

the damaged layers without inducing further etching damage. Tertiarybutylchloride-based *in situ* etching may serve as an alternative etching method to dry etching with reduced etching damage. In terms of devices, regrown p-n junctions with low leakage currents and vertical junction field-effect transistors were demonstrated. Further improvements in selective area regrowth and associated devices can be expected using regrowth optimization and regrowth interface engineering via surface treatments and low-damage etching. These results represent an important step towards realizing selective area regrowth and doping for high performance GaN power electronics devices and systems.

Keywords: Gallium nitride; Power electronics; Vertical power devices; Selective area doping and regrowth; interface engineering

Introduction

Wide bandgap semiconductor gallium nitride (GaN) has been extensively researched as the emerging workhorse for the next-generation efficient power electronic devices and systems due to its wide bandgap, high critical electric field, fast switching speed, and high Baliga's figure of merit [1–12]. Fig. 1a compares the performance of different semiconductors for power electronics applications, where GaN devices are expected to outperform their Si counterparts. In order to unleash the full potential of GaN, vertical GaN power devices grown on bulk GaN substrates (Fig. 1b) have been widely investigated in recent years, including Schottky barrier diodes [13–21], p-n diodes [22–42], other advanced power rectifiers [43–47] and transistors [48–58] such as current aperture vertical electron transistors (CAVETs), trench metal–oxidesemiconductor field-effect transistors (MOSFETs), and fin field-effect transistors (FinFETs). In the early stage of GaN power devices development, lateral devices such as the GaN high electron mobility transistors (HEMTs) were first proposed and demonstrated usually on foreign substrates such as sapphire and SiC. In lateral devices, the current flows laterally, and the breakdown voltage is held laterally. Compared with lateral devices, vertical devices can offer tremendous advantages, including higher voltages, higher currents, smaller chip area, better thermal management, no surface-related issues, and avalanche capability [1,2,7]. However, one of the most critical building blocks that is still missing for vertical GaN power devices is laterally patterned GaN p-n junctions, the schematic of which is illustrated in Fig. 2a. These laterally patterned p-n junctions are the basis for many advanced GaN power devices and edge terminations, such as vertical junction field-effect transistors (VJFETs) (Fig. 2b), junction termination extension (JTE) (Fig. 2c), and junction barrier Schottky (JBS) or merged pn/Schottky (MPS) diodes (Fig. 2d).

Laterally patterned p-n junctions (Fig. 2a) can be realized by selective area doping via two methods: ion-implantation and epitaxial regrowth. After decades of development, ion implantation has become a mature technology in Si and SiC [59–61], and similar Si and SiC structures and devices to those in Fig. 2 have been demonstrated. However, ion implantation still remains one of the biggest hurdles for GaN power devices [16]. This is mainly attributed to the following reasons. Ion bombardment during the ion implantation process can cause severe material damage, and subsequent high temperature annealing (usually >1000 °C) is required to recover the damage. In addition, some of the implanted atoms may be at interstitial sites, and high temperature annealing can restore them to the correct substitutional sites to activate them as dopants [61,62]. However, the high temperature annealing can decompose GaN when above 900 °C and cause killer defects and surface degradation [63,64]. Several methods have been proposed to alleviate GaN decomposition at high temperatures, including AlN capping layers, multicycle rapid thermal annealing, and ultra-high annealing pressure [65–67]. Furthermore, the conductivity of implanted p-GaN is still much lower than the epitaxially grown p-GaN [26,43], which can adversely impact device performance.

Epitaxial regrowth or selective area regrowth is regarded as a promising alternative route to realizing laterally patterned GaN p-n junctions. However, regrown GaN p-n junctions usually suffer from high leakage currents and low breakdown voltages [68,69]. In this review, challenges and recent progress of selective area regrowth and doping for vertical GaN power transistors are presented. This review is organized as follows. Section 2 will discuss the general regrowth process and the regrowth dynamics in trenches with two growth modes revealed. The effects of trench geometries, growth methods, and bulk substrates will be discussed. Section 3 will focus on several important material characterization techniques for the selective area regrowth, including cathodoluminescence (CL), dopant profiling via secondary electrons (SEs) in scanning electron microscopy (SEM), atom probe tomography (APT), the regrowth interface characterizations using capacitance–voltage (*C*–*V*) measurements, secondary ion mass spectrometry (SIMS) and transmission electron microscopy (TEM), and electron holography and scanning probe microscopy (SPM) for the electrostatic potential profile at the regrowth interface. These techniques serve as the foundation for the regrowth study. Section 4 will introduce three novel etching technologies to reduce etching damage or replace the state-of-the-art dry etching method, including low-power dry etching, photoelectrochemical (PEC) wet etching, atomic layer etching (ALE), and *in situ* and selective area etching. The effects of these etching methods on the performance of regrown devices will be discussed. Section 5 will show several demonstrated regrown devices, including planar regrown p-n junctions and the vertical junction field-effect transistors (VJFETs).

Selective area regrowth

Regrowth process

In order to achieve selective area doping by regrowth, dry etching is an inevitable process to form the selective regions/trenches for regrowth. However, the etch-then-regrow process is very

Please cite this article in press as: H. Fu et al., Materials Today, (2021), https://doi.org/10.1016/j.mattod.2021.04.011

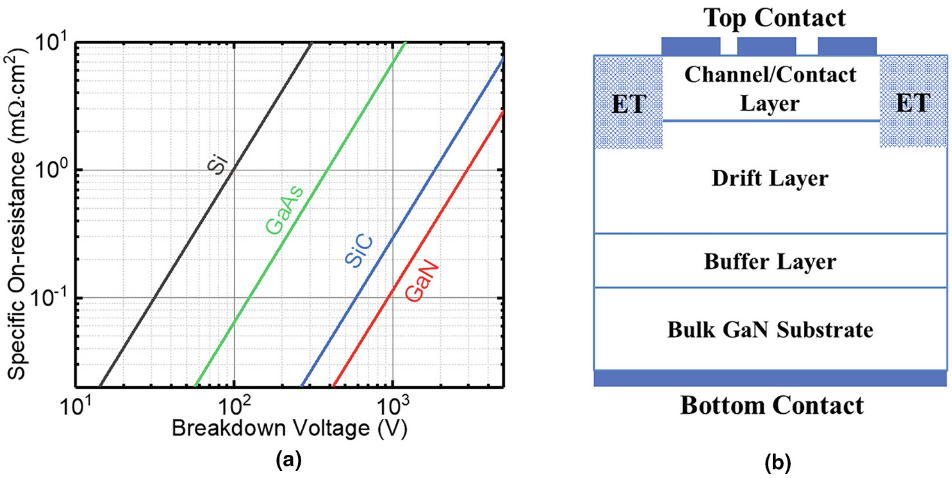

FIGURE 1

(a) Benchmark plot of specific on-resistance versus breakdown voltage for different semiconductors for power electronics applications. (b) Schematic of vertical GaN power devices on bulk GaN substrates, including channel/contact layer, edge termination (ET), drift layer, and buffer layer.

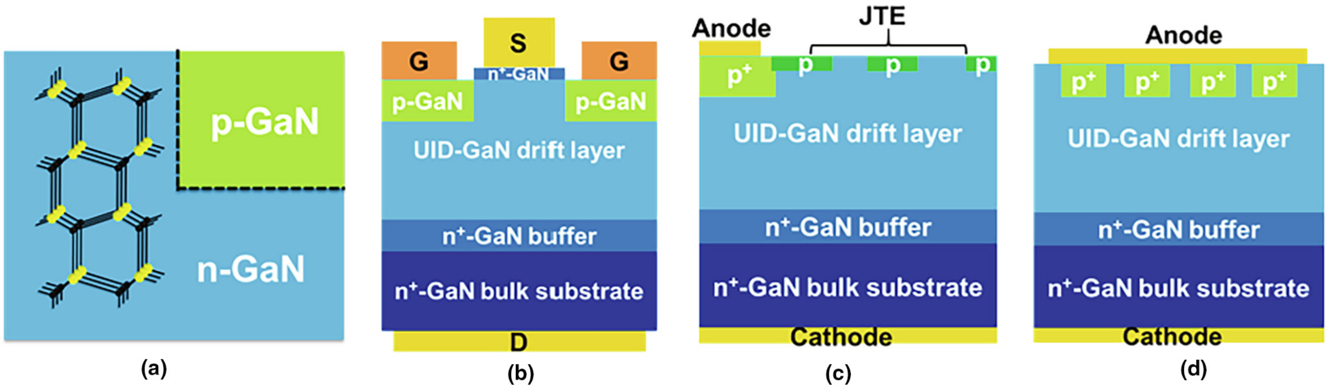

FIGURE 2

(a) Schematics of laterally patterned p-n junctions by selective area doping. (b) Vertical junction field effect transistors (VJFETs); (c) Junction termination extension (JTE); (d) Junction barrier Schottky (JBS) or merged pn/Schottky (MPS) diodes.

challenging and induces interface impurities. Even without any etching, the regrowth process still introduces a high concentration of impurities at the regrowth interface, such as silicon (Si), carbon (C), and oxygen (O). Thermal desorption of these impurities through annealing in metal–organic chemical vapor deposition (MOCVD) or molecular beam epitaxy (MBE) has been used for *in situ* cleaning. Annealing in NH_3 at 700–800 °C or multistep alternating growth and annealing under vacuum at 780 °C could effectively remove C and O [70,71]. However, the residual Si was not able to be removed by these methods. These impurities may not be a problem for regrowing n-type GaN since Si and O are shallow donors for n-type doping. However, these impurities are highly undesired for regrowing p-GaN since they can compensate acceptors and reduce hole concentrations. Furthermore, the dry etching process can also introduce etching damage at the regrowth interface, causing deep-level defect/trap states. Due to these issues, regrown GaN p-n junctions have suffered from high leakage and premature breakdown.

Fig. 3a shows a typical regrowth process in MOCVD, including three steps, i.e., before regrowth, ramp-up with temperatures and gases, and regrowth. An n$^+$-GaN buffer layer and an unintentionally doped (UID) GaN were first grown on GaN substrates. Then the sample was taken out of the reactor for processing and then reloaded into the reactor. To study the effect of growth conditions on the regrowth process, four different combinations of growth gases were used for the ramp-up step, including $N_2/NH_3/H_2$, N_2, N_2/trimethylgallium (TMGa, 6 sccm), and N_2/TMGa (12 sccm). Then a UID-GaN layer was regrown on top of the sample. Fig. 3b shows the SIMS profiles of the regrown UID-GaN with different gases in the ramp-up step. Si peaks were observed in all samples. Although Ga-rich condition is helpful to reduce Si incorporation [72], the introduction of TMGa in the ramp-up step led to a significant increase in Si, O, and C. Compared with other conditions, the sample under the $N_2/NH_3/H_2$ showed the lowest Si concentration at the regrowth interface. It has been reported that reducing the sample's exposure time to air can reduce the residual Si, for

Please cite this article in press as: H. Fu et al., Materials Today, (2021), https://doi.org/10.1016/j.mattod.2021.04.011

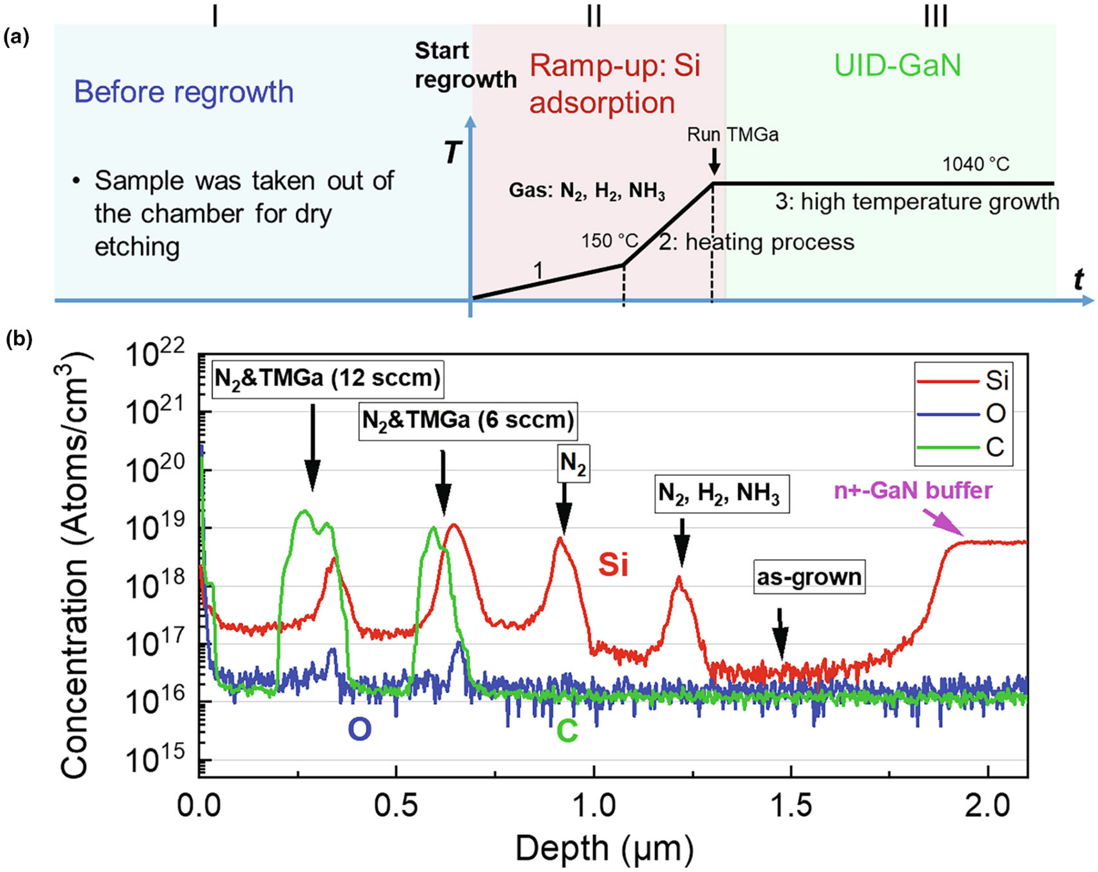

FIGURE 3

(a) Schematic of the regrowth process for regrown UID-GaN in MOCVD. (b) SIMS profile of the regrown UID-GaN with different ambient gases during the ramp-up step.

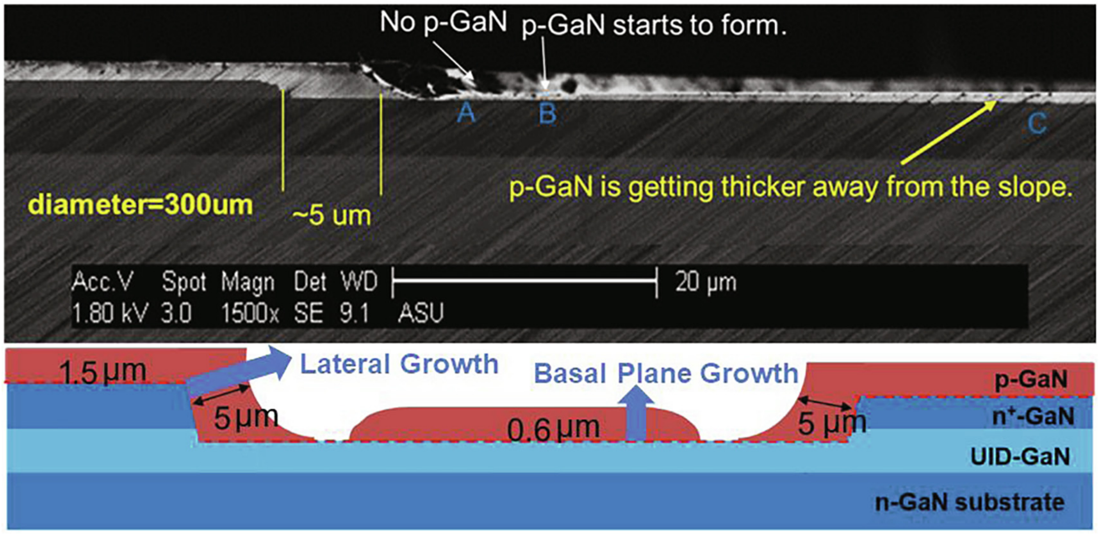

FIGURE 4

Top: SEM image of selective area regrowth in a trench. Bottom: Schematics of the thickness distribution of regrown p-GaN in different regions: trench, sidewalls, and mesa. The arrows indicate growth directions.

example, putting the sample in N_2 box during processing [73]. Surface treatment and etching conditions before regrowth are also important factors that can affect the interfacial impurity concentration, which will be discussed in the following sections. Overall, the residual Si at the interface is still an intractable issue for regrowth, and its origin is still unclear.

Please cite this article in press as: H. Fu et al., Materials Today, (2021), https://doi.org/10.1016/j.mattod.2021.04.011

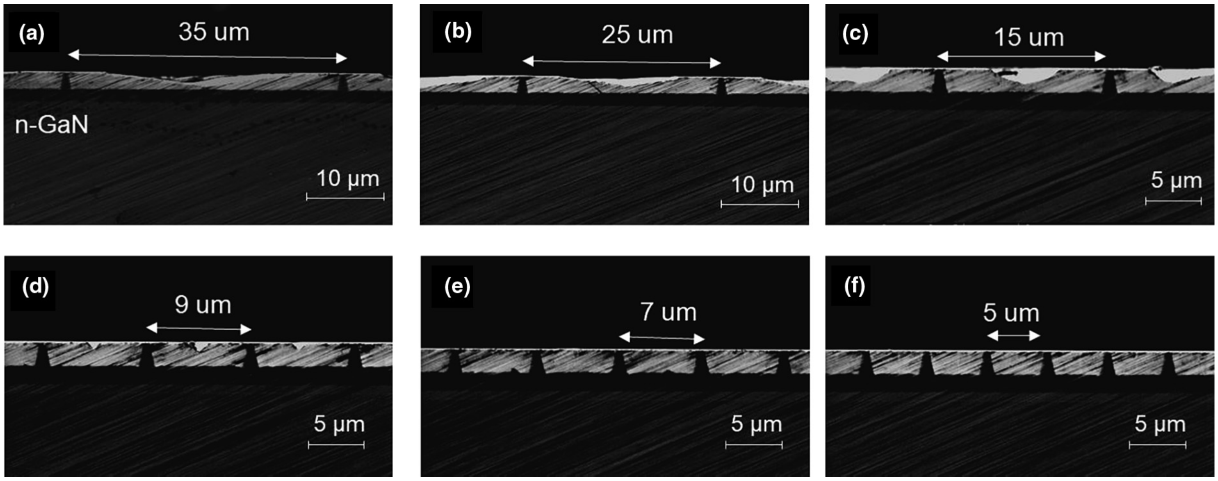

FIGURE 5

SEM images of selective area regrowth in trenches with different widths. (a) 35 µm; (b) 25 µm; (c) 15 µm; (d) 9 µm; (e) 7 µm; (f) 5 µm.

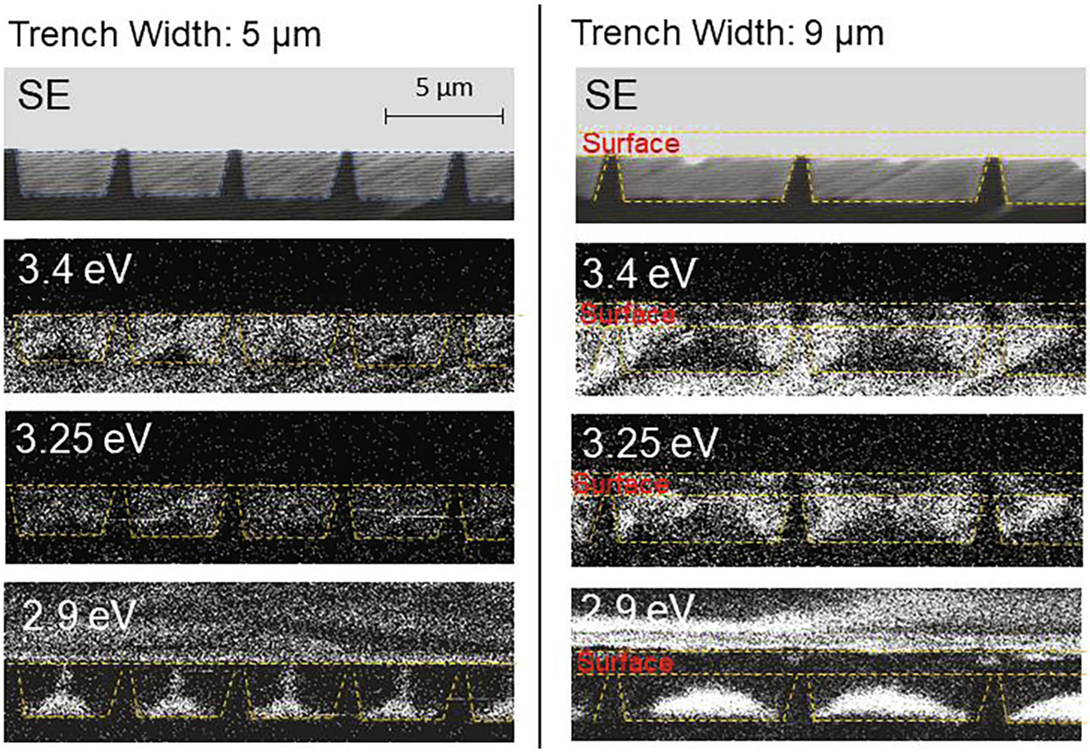

FIGURE 6

Comparison of SE images and monochromatic CL mappings for different luminescent energies (3.4 eV, 3.25 eV, and 2.9 eV) for selective area regrowth in trenches with trench widths of 5 µm (left) and 9 µm (right). The right sample is slightly tilted so that part of the surface is also in view. SE: secondary electron. Reprinted from Ref. [79], with the permission of AIP Publishing.

Regrowth on trench structures

The laterally patterned p-n junctions were grown on n^+-GaN substrates by MOCVD via an etch-then-regrow process. First, a UID-GaN layer was grown on the substrate. Then, the samples were unloaded from the MOCVD reactor, and trenches were formed by inductively coupled plasma (ICP) etching. Finally, the samples were reloaded into the MOCVD reactor, and p-GaN was regrown. It should be noted that this process is a maskless regrowth process since previous studies showed that regrowth with SiO_2 or Si_3N_4 masks resulted in the introduction of unintentional impurities such as Si or O and led to n-type conductivity [74–76]. Fig. 4 shows a representative SEM image of regrown p-GaN in a trench. The p-GaN appeared bright, and the n-GaN had dark contrast; the reasons for this contrast difference are discussed later [77]. The regrowth of p-GaN in the trench was nonuniform. The p-GaN on the trench sidewall was much thicker than other regions due to the faster lateral growth compared with the basal plane growth. This larger growth rate could

Please cite this article in press as: H. Fu et al., Materials Today, (2021), https://doi.org/10.1016/j.mattod.2021.04.011

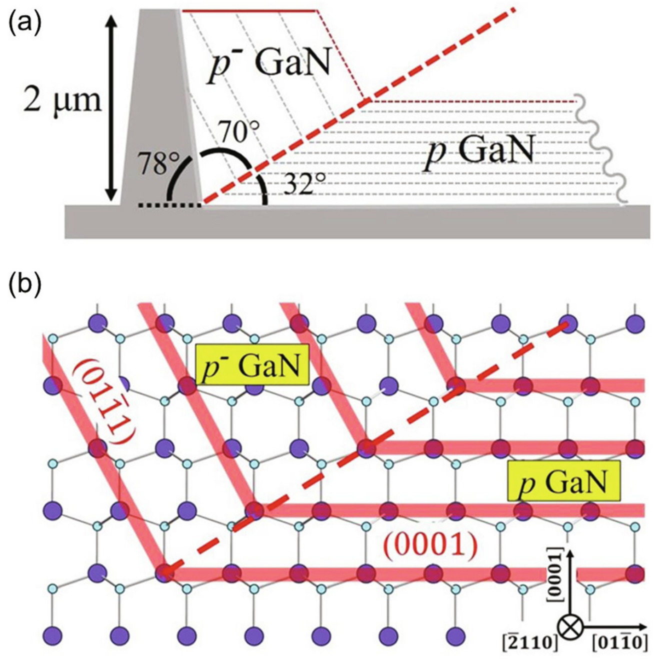

FIGURE 7

Lateral growth versus vertical growth in p-GaN regrown on trenches. (a) Schematic cross-section showing the two characteristic regions observed in the CL image with a 32° boundary, with p-GaN growth parallel to the basal plane and p$^-$-GaN growth from the sidewall. (b) The atomic arrangement of the lattice indicating the 32° boundary for coincident lateral growth on $\{01\bar{1}1\}$ facets and on $\{0001\}$ basal planes. Reprinted from Ref. [79], with the permission of AIP Publishing.

result in much lower Mg or acceptor concentrations in the sidewall.

To clarify the growth dynamics, selective area regrowth was performed in trenches with different trench widths and depths. With decreasing trench width, the thickness of the regrown p-GaN became more uniform throughout the trench, as shown in Fig. 5. For a trench width of < 9 μm, the p-GaN region in the trench was rather flat. This is because, in a narrow trench, the growth fronts from the trench sidewall and the basal plane can coalesce faster and form a united growth front, leading to uniform p-GaN growth. Cathodoluminescence (CL) was used to map the Mg distribution in the trenches. It has been identified that strong CL emission at 2.9 eV is a reliable indicator for high acceptor concentrations [78]; more details on this topic are discussed later. In the 2.9-eV CL mapping (Fig. 6), the central region of the trench was much brighter than the sidewall [79], indicating that the acceptor concentration in the former was higher. With increasing trench width, the central region of the trench became brighter, which suggested that the basal plane growth was becoming more dominant.

Understanding of the physical basis for these observations was obtained by considering the lateral growth from the sidewall and the vertical growth from the basal plane of the trench [79]. Surface steps of the growth front and their aggregation into supersteps lead to a competition between step flow that results from the growth on microfacets and vertical growth from basal planes [80]. Monochromatic CL images show that growth on basal planes exhibited a strong 2.9 eV emission, while growth from the sidewall facets did not [81]. The interface between these regions formed an angle of about 32° with the basal plane, as shown in the lattice structure in Fig. 7 [79]. The $\{01\bar{1}1\}$ and $\{0001\}$ facets are the most stable in GaN and have been observed in epitaxial lateral overgrowth studies [82]. The sidewall facet can be thought of as a highly tilted facet composed of a high density of basal-plane steps, where each step serves as an effective site for adatom capture and facilitate lateral growth. The presence of Mg on the $\{01\bar{1}1\}$ facet can increase the adsorption of Ga and promote the accumulation of Ga adatoms in the vicinity of the sidewall. The lateral growth rate was found to be two times larger than the vertical growth rate. Therefore, with the same amount of Mg acceptors available during growth, the acceptor concentration near the sidewall will be smaller than that at the central region of the trench. This is confirmed by the CL analysis, in which the vertical growth region was p-type, while the lateral growth region was semi-insulating with a low acceptor concentration. In addition, previous studies also showed that Mg incorporation efficiency was different on different facets.[78,81] Overall, the trench width must be optimized (not too wide nor too narrow) (1) to ensure uniform p-GaN thickness inside the trenches, and (2) to maximize basal plane growth to obtain the highest acceptor concentrations in the trenches of the regrown p-GaN.

The effect of trench depth on selective area regrowth was also investigated, as shown in Fig. 8. For a shallow trench with a depth of 0.3 μm, no clear evidence of lateral growth from the sidewall was found by CL mapping. As the trench depth increased, the sidewall surface area also increased. As a result, the area of lateral growth with low acceptor concentrations also increased, as confirmed by the reduced CL emission intensity at 2.9 eV near the sidewall. In addition, Fig. 9a shows that the reverse current leakage of the selective area doped p-n junctions also increased with increasing trench depth. The model shown in Fig. 9b was proposed to explain this trend. According to the CL results, the sidewall in deeper trenches had a lower acceptor concentration, resulting in a p$^-$-GaN or even intrinsic region. Therefore, the junction barrier near the sidewall may be reduced, creating a leakage path. This issue may be solved by adjusting the growth mode or by increasing the acceptor doping or activation efficiency along the sidewall. In short, using shallow trenches for selective area growth may be beneficial for reducing the reverse leakage of the selective area doped p-n junctions.

MOCVD and MBE regrowth comparison

MOCVD growth of GaN is typically performed at high temperatures (>950 °C) with NH_3 as the precursor for N. There are significant challenges, however, when the device structure involves p-GaN buried by subsequent n-GaN growth, such as current aperture vertical electron transistors (CAVETs) [1,2], trench-MOSFETs [48–53], and tunnel junctions (TJs) [83]. P-type conductivity of buried p-GaN is often hindered because active H atoms from the decomposition of NH_3 or H_2 in n-GaN growth are able to diffuse backward and passivate Mg dopants when growing n-GaN under high temperatures [84]. After growth, activation of the buried p-GaN becomes difficult due to a high diffu-

Please cite this article in press as: H. Fu et al., Materials Today, (2021), https://doi.org/10.1016/j.mattod.2021.04.011

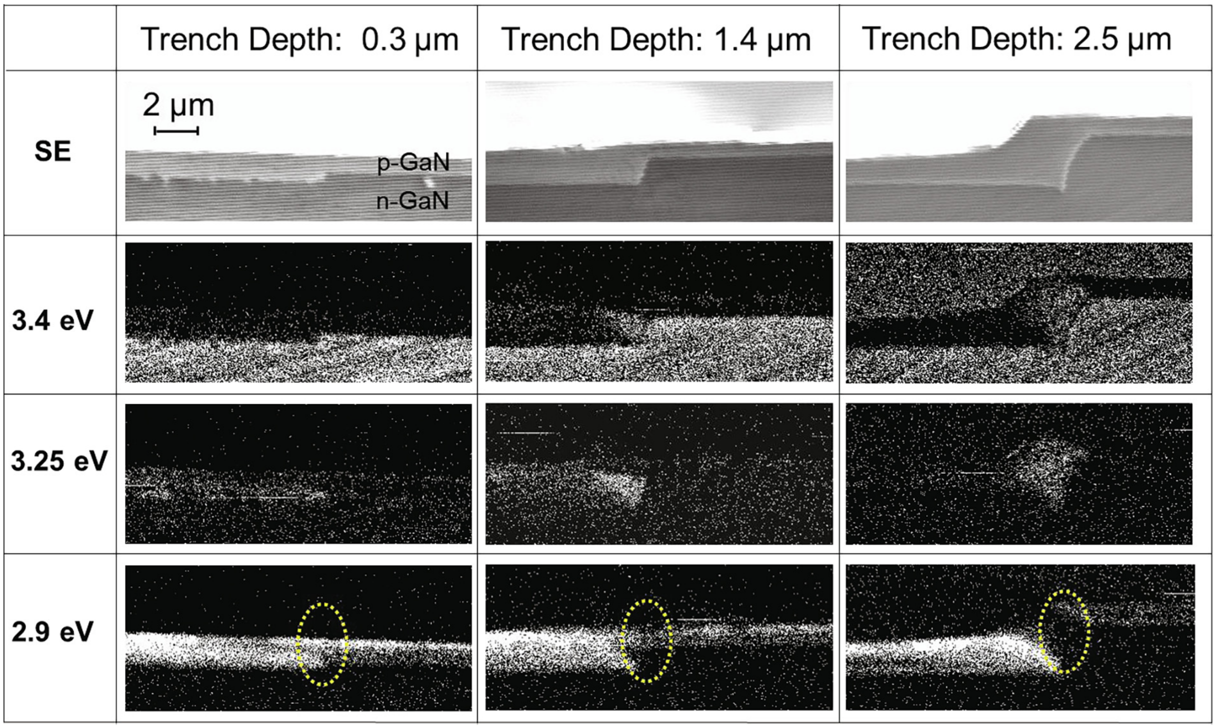

FIGURE 8

SE images and monochromatic CL mapping for different luminescent energies (3.4 eV, 3.25 eV, and 2.9 eV) for selective area regrowth in trenches with different depths (0.3 μm, 1.4 μm, and 2.5 μm). The circled regions indicate the sidewall.

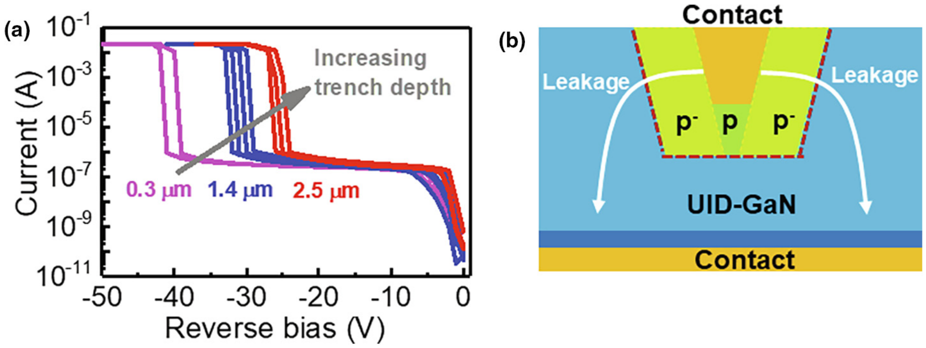

FIGURE 9

(a) Reverse leakage characteristics for selective-area doped p-n junctions with different trench depths. (b) A proposed model to explain the reverse leakage of selective-area doped p-n junctions. The p-contacts are Pd/Ni/Au, and the n-contacts are Ti/Al/Ni/Au.

sion barrier of H atoms in the n-GaN [85]. Attempts have been made to activate buried p-GaN laterally through mesa sidewalls [86]. Moreover, Mg in the buried p-GaN can diffuse into the overlayers, which could adversely affect the properties of two-dimensional electron gas (2DEG) in the CAVET like structures. Similarly, defects generated during the ion-implantation process to form the current blocking layer (CBL) in CAVET structure were also reported to diffuse to the active region and cause the current collapse in the on-state of operation [2].

MBE growth of GaN is carried out in a hydrogen-free environment and is expected to provide solutions to the problems mentioned above. MBE overgrowth on MOCVD-grown Mg-doped GaN left the p-GaN remaining activated [87]. MBE-regrown trench-MOSFET [88,89] and PolarMOS have been demonstrated [90]. Additionally, MBE employs much lower growth temperatures (<800 °C), which alleviates the diffusion of Mg atoms and point defects to active regions. Chowdhury et al. reported dispersion-free CAVET structures with Mg implantation and MBE-regrown channels [2]. In addition, MBE-regrown p-n junctions showed a breakdown voltage of 1.1 kV, a specific on-resistance of 3.9 mΩ·cm^2, and a turn-on voltage of 3.9 V [91]. In these MBE regrown devices, the less-than-ideal device performance was mainly due to defects and interface charges at the regrowth interfaces [88–91].

In order to achieve non-planar or lateral p-n junction devices, selective area growth and doping is a very promising approach, as mentioned above. Selective area regrowth of GaN using MBE reactor has been reported by several groups. Different mask

Please cite this article in press as: H. Fu et al., Materials Today, (2021), https://doi.org/10.1016/j.mattod.2021.04.011

materials have been tested, including Ti, SiO_2, and SiN_x [92–94]. High growth temperatures and low V/III ratios facilitated the desorption of Ga atoms on the mask [93,94] and improved the selectivity. Good selectivity and surface morphology were only achieved on a periodic array of nanocolumn structures. The low V/III condition led to a porous surface morphology at high temperatures for large-area devices [92]. Additionally, spike-like structures at the edge of masks were observed due to the short diffusion length of adatoms [90,95].

Effects of bulk substrates

Recent developments in crystal growth techniques such as hydride vapor pressure epitaxy (HVPE) and ammonothermal methods have led to the availability of bulk GaN substrates with defect densities lower than $\sim 10^6$ cm^{-2}. The recent development of bulk GaN substrates via the two methods is described in [96]. HVPE GaN substrates are commercially available up to 4 inch. They are produced by growing thick GaN epilayers on foreign substrates such as sapphire and use the thick GaN epilayers as the template for the next growth via an iterative fashion to improve crystal quality. Ammonothermal GaN substrates are currently only available mostly in 1 inch and up to 2 inch. But they have better crystal quality than HVPE substrates since they are grown from single-crystal GaN seed via a melt approach. In addition, Raghothamachar et al. [97] and Liu et al. [98] used synchrotron X-ray topography (XRT) to study the dislocations in the HVPE and ammonothermal GaN substrates. They found that HVPE substrates showed a heterogeneous distribution of dislocations that contained low threading dislocation areas between strain centers with high threading dislocation densities. On the other hand, ammonothermal substrates had a much lower defect density than HVPE substrates. They were dominated by threading mixed dislocations but free of basal plane dislocations. Epitaxial GaN layers can be grown with much reduced defect density using such bulk substrates [99], and have enabled the fabrication of vertical GaN devices with high breakdown voltages [100]. Nevertheless, the occurrence of random defects is still liable to cause degraded device performance and irreproducible device behavior. Since such defects cannot be totally eliminated, fabrication of devices for high power applications should concentrate on areas with minimal defects and avoid regions with high defect densities in order to minimize defect-related current leakage and possible device breakdown. The substrate morphology has a critical influence on the subsequent layer quality and the corresponding device performance.

Fig. 10a–c compares XRT images of GaN thin films that were grown on HVPE GaN substrates from two different sources and one grown on an ammonothermal substrate. The XRT image of GaN grown on HVPE substrate-1 showed discontinuous, mostly vertical features, whereas the XRT image of GaN grown on HVPE substrate-2 showed a two-dimensional array of dark spots. In both cases, the surface features were roughly equally spaced with lateral separations of ~1 mm. In comparison, the XRT image of GaN grown on the ammonothermal substrate revealed no significant surface features. One of the GaN layers grown on HVPE substrate-2 was surface etched with ICP plasma, and SEM images revealed micron-scale defects in the form of inverted hexagonal-pyramid pits at the locations of each dark spot. In contrast, areas away from these defective regions showed no visible flaws. In device studies, devices that overlapped with the dark spots performed poorly, whereas devices fabricated away from these regions generally had much better performance. In marked contrast, not all devices fabricated on the ammonothermal substrate performed well. Fig. 10d shows several locations where devices were fabricated on the ammonothermal GaN substrate. The red circles indicate locations of fabricated devices that had low breakdown voltages, whereas the white circles indicate the areas of devices having typical high breakdown voltages. Fig. 10e shows a plan-view SEM image of such a device showing significant surface damage after breakdown, while Fig. 10f shows a device without visible surface damage after being stressed to high reverse biases. Overall, the HVPE-grown substrates showed surface features in XRT images that clearly should be avoided during device fabrication. Conversely, the absence of any observable surface features for the ammonothermal substrates makes it challenging to predict device behavior. Furthermore, most of the current selective area regrowth work is based on HVPE GaN substrates due to their relatively early commercial availability. Future work is ongoing to study how the crystal conditions of bulk GaN substrates affect the selective area growth.

Materials characterization

Materials characterization techniques play a critical role in selective area regrowth and doping. They provide powerful tools to guide optimization in the design and growth and to understand the performance of regrown GaN devices. In this section, several materials characterization techniques that are instrumental to selective area regrowth and doping are discussed, including CL for the acceptor distribution in mesa structures, dopant profiling via SEs and ATP for both lateral and vertical structure at the submicron scale, regrowth interface study by C–V measurements, SIMS and TEM for interfacial charges and impurities, and electron holography and SPM for electrostatic potential profiles at the regrowth interfaces. These methods reveal materials challenges in selective area regrowth and doping and physical mechanisms for large leakage currents in regrown devices and provide a route for future improvements.

Cathodoluminescence

Fig. 11a shows a typical growth and fabrication process to produce laterally patterned GaN p-n junctions. There are two growth directions involved: the basal plane growth on the upper and lower mesa flat regions and lateral growth on inclined crystal planes on the mesa sidewall. It has been reported that crystal orientations in GaN significantly affect acceptor incorporation efficiency [101–103]. Thus, it is essential to have a good understanding on the acceptor distribution in the mesa structure. For example, in GaN VJFETs, the acceptor concentration in the p-GaN gate determines the operation of devices, in particular, whether the gate can pinch off the channel at zero bias. The traditional SIMS method cannot give reliable chemical analysis on this structure due to its limited lateral spatial resolution. Liu et al. [78] used CL spectroscopy to study optical properties of regrown p-GaN over mesa structures at the sub-micron scale and their correlation with acceptor concentrations and electronic properties. The CL was carried out in a JEOL 6300 SEM

Please cite this article in press as: H. Fu et al., Materials Today, (2021), https://doi.org/10.1016/j.mattod.2021.04.011

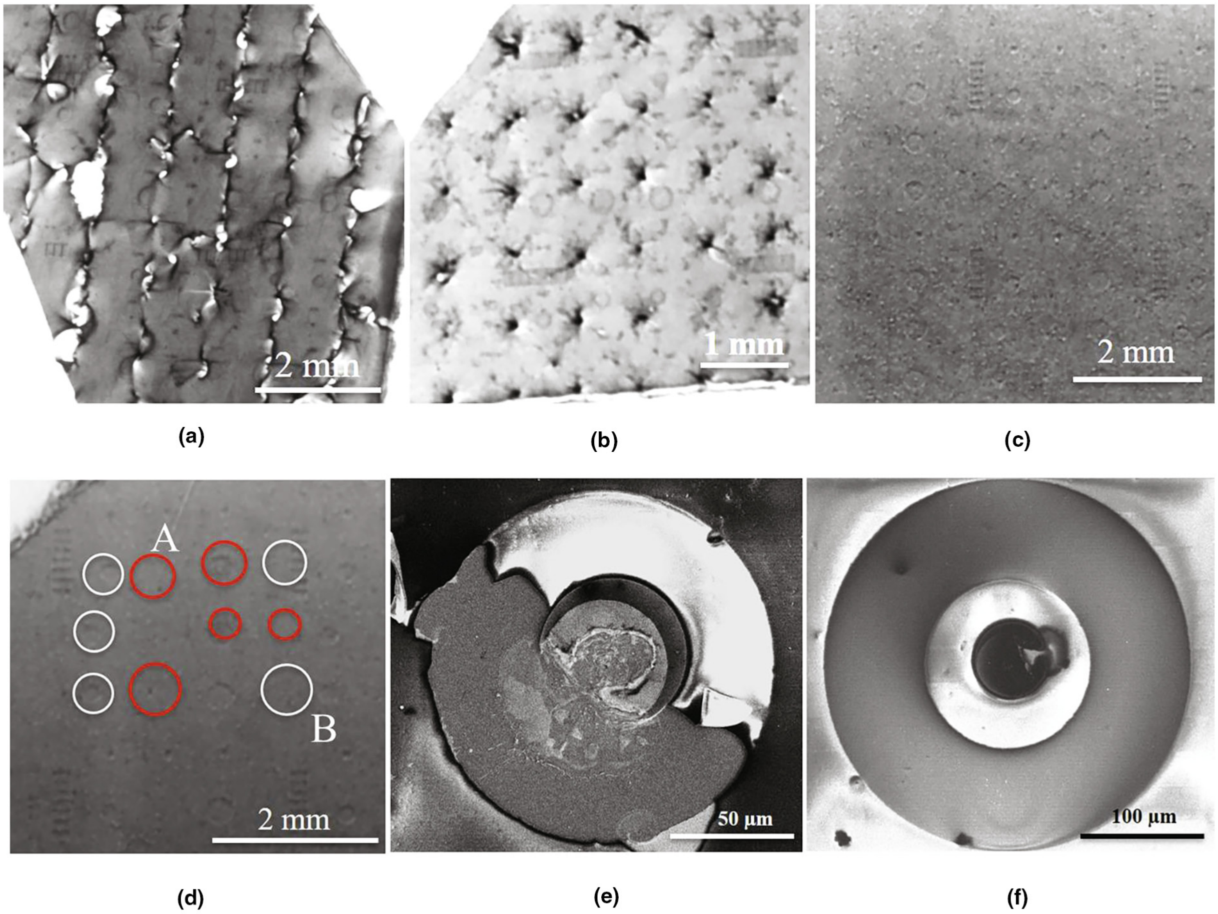

(a) (b) (c)

(d) (e) (f)

FIGURE 10

XRT images from three different types of bulk GaN substrates: (a) GaN film on HVPE- substrate-1 showing the presence of dark discontinuous lines; (b) GaN film on HVPE substrate-2 showing a two-dimensional array of dark spot-like features; and (c) GaN film on ammonothermal substrate not showing any noticeable surface features. (d) XRT image showing locations of fabricated devices, as marked by circles: red circles represent device locations having low breakdown voltages; white circles represent device locations having high breakdown voltages. (e) Plan-view SEM image of device marked as ‘A’ in (d), showing substantial surface damage after being stressed to breakdown at a low reverse bias; (f) Plan-view SEM image of device marked as ‘B’ in (d), showing no visible surface damage after stressing to high reverse biases.

equipped with a monochromator and a photomultiplier. The epitaxially regrown structure investigated is shown in Fig. 11b, and its SE image is shown in Fig. 11c. Two modes of CL were used. The first one was CL mapping, where the monochromator was set to a certain wavelength, and a spatial variation of luminescence intensity was obtained. Fig. 11d and 11e present the CL mapping at 3.25 eV and 2.9 eV, respectively. The luminescence in the 3.25-eV CL mapping was relatively uniform. But the 2.9-eV CL mapping clearly exhibited nonuniform luminescence distribution, where the sidewall had much weaker emission intensity.

To better understand this phenomenon, the spot mode CL was utilized. In this mode, the electron beam was fixed at the desired sample location, and the CL spectra were recorded over a specific wavelength range. The interaction volume of the electron beam in the spot mode CL (in this work, 100 pA and 7 kV) was ~400 nm in diameter, rendering sub-micron spatial resolution. Fig. 12a shows a lower magnification version of Fig. 11e. Five regions can be identified: upper mesa, sidewall, lower mesa top, lower mesa bottom, and lower mesa away from the sidewall. The upper mesa and the lower mesa away from the sidewall show uniform and strong emission, whereas the emission near the sidewall is nonuniform. The emission spectra of the five regions in Fig. 12b were obtained using the spot mode CL. Three peaks were observed: 3.4 eV, 3.25 eV, and 2.9 eV. The 3.4 eV is due to the near-band-edge excitonic transition, 3.25 eV is the shallow donor to Mg-acceptor transition, and 2.9 eV is the deep donor to Mg-acceptor transition [104–106]. The CL spectra of the sidewall of the lower mesa top were dominated by the 3.4-eV and 3.25-eV peaks, while those of the upper mesa, lower mesa bottom, and lower mesa away from the sidewall showed strong peaks at 2.9 eV.

To correlate the CL spectra with acceptor concentrations, three reference samples with Mg concentrations of 1.3×10^{19} cm^{-3}, 3.1×10^{19} cm^{-3}, and 6.3×10^{19} cm^{-3} were grown and characterized, as shown in Fig. 12c. It was found that the 2.9 eV peak became dominant, and its intensity increased with increasing acceptor concentration, while the intensities of the other two high energy peaks decreased. Thus, the weak emission at 2.9 eV is related to the low acceptor concentration. From a comparison between Fig. 12b and 12c, it was found that the side-

Please cite this article in press as: H. Fu et al., Materials Today, (2021), https://doi.org/10.1016/j.mattod.2021.04.011

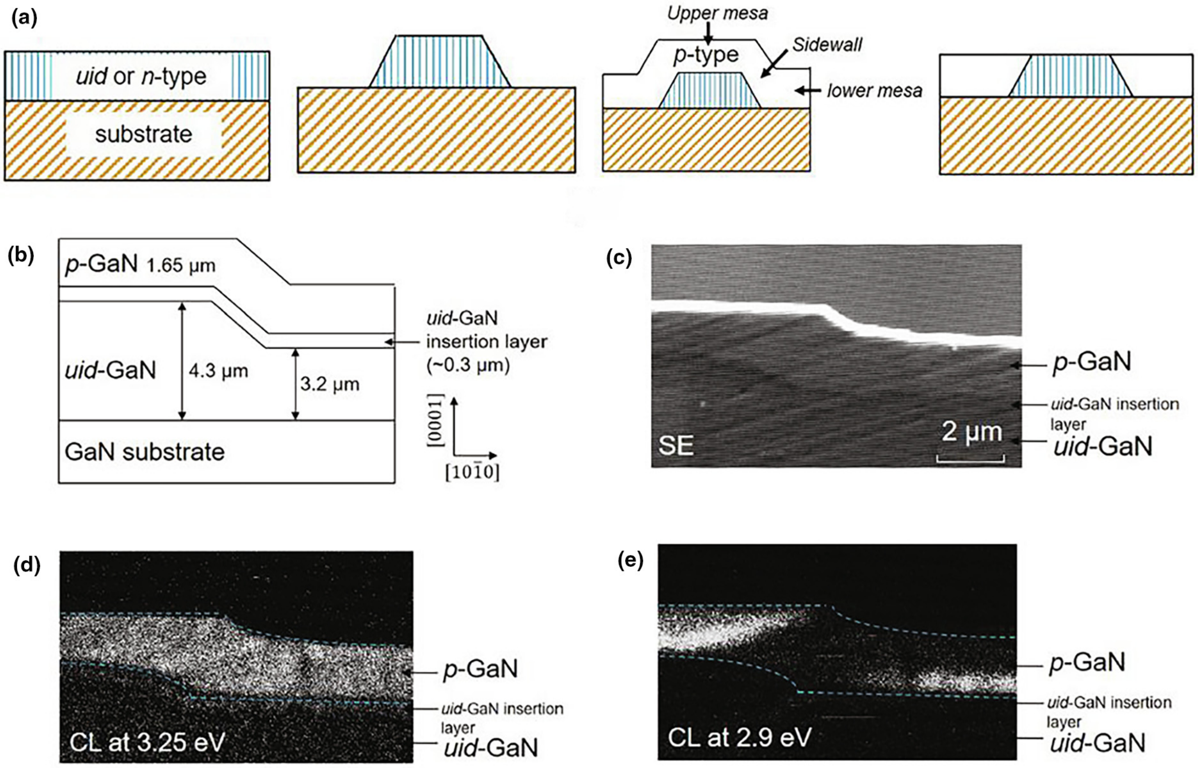

FIGURE 11

(a) Growth and fabrication steps to produce selective-area doped p-n junctions in an etch-then-regrowth process. From left to right: UID- or n-GaN growth, mesa etching, p-GaN regrowth, and upper-mesa p-GaN removal. (b) Regrown p-GaN/UID-GaN mesa structures before etching. (c) SE image of the mesa structure. Monochromatic CL images at (d) 3.25 eV and (e) 2.9 eV. The dash lines indicate the boundaries between the regrown p-GaN and UID-GaN. Reprinted from Ref. [78], with the permission of AIP Publishing.

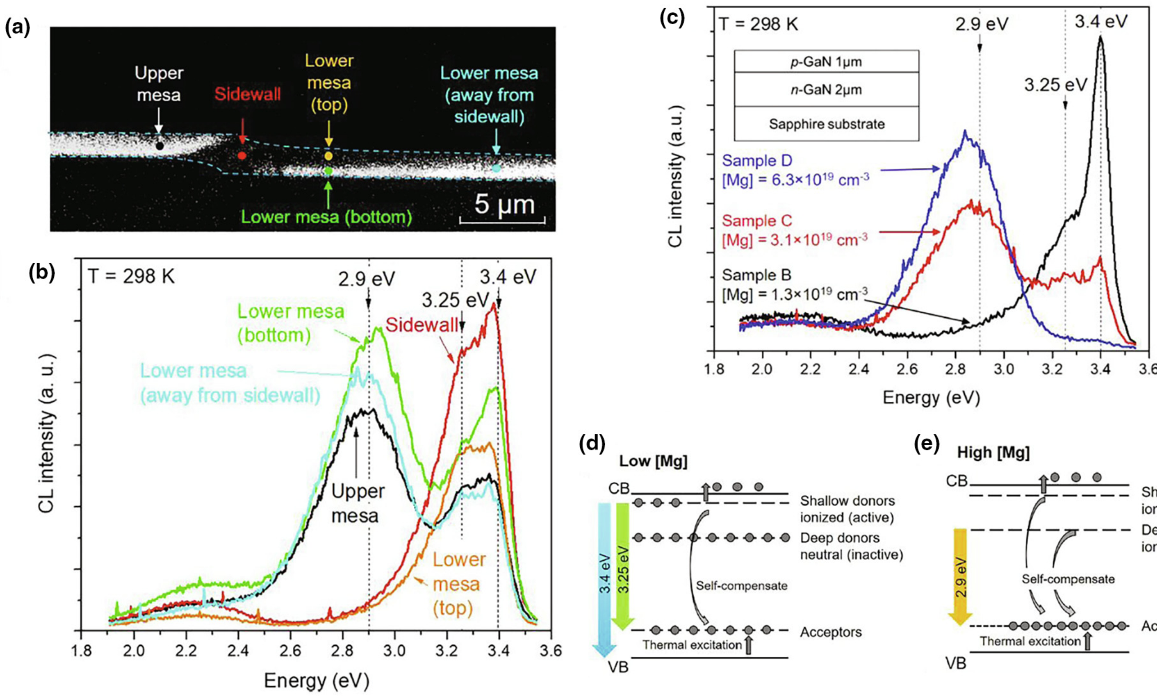

FIGURE 12

(a) Monochromatic CL mapping at 2.9 eV for the regrown p-GaN/UID-GaN mesa structure with different regions labeled. (b) Spot-mode CL spectra in different regions in the regrown p-GaN as labeled in (a). (c) CL spectra of reference p-GaN samples with different Mg concentrations. Proposed mechanisms for different cathodoluminescence characteristics of p-GaN with (d) low [Mg] and (e) high [Mg]. Reprinted from Ref. [78], with the permission of AIP Publishing.

Please cite this article in press as: H. Fu et al., Materials Today, (2021), https://doi.org/10.1016/j.mattod.2021.04.011

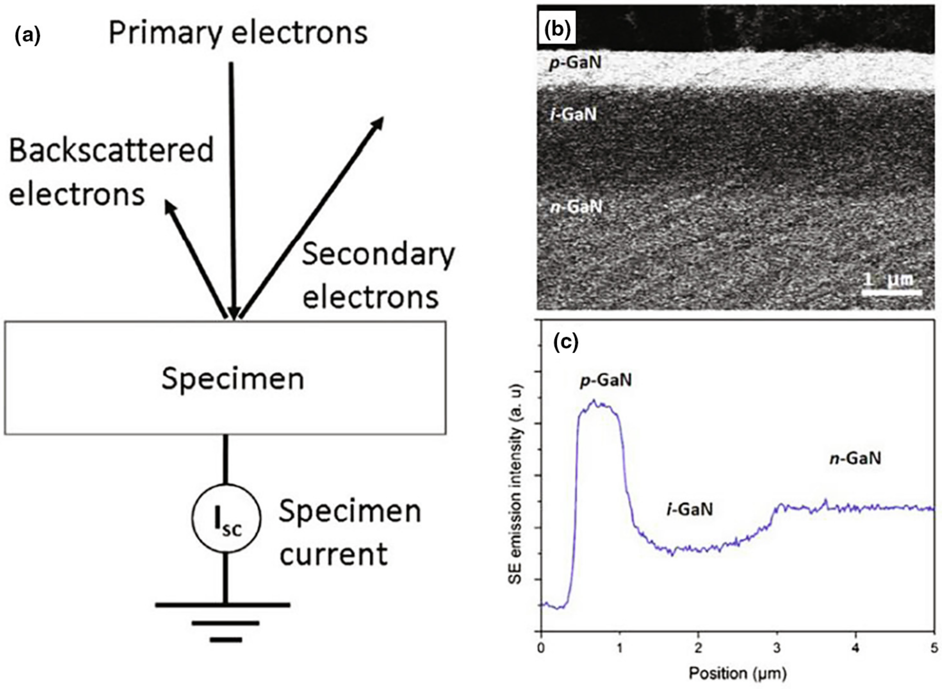

FIGURE 13

(a) Schematics of different types of electrons flowing in and out of a specimen in an SEM. The specimen current is used to maintain charge neutrality in a semiconductor. SE image (b) and the SE emission intensity profile (c) of a GaN *p-i-n* structure at a beam voltage of 2 kV and a beam current of 53 pA. Reprinted from Ref. [77], with the permission of AIP Publishing.

wall and the lower mesa top suffered from acceptor deficiency. Liu et al. [74] proposed a mechanism to explain the different CL spectra at low and high Mg concentrations. Initially, both the shallow and deep donor states are occupied by electrons. They can lose these electrons either to the conduction band by thermal excitation or to acceptors via self-compensation to become ionized. The ionized shallow donors are involved in the 3.25-eV transition, and the ionized deep donors participate in the 2.9-eV transition. At low Mg concentration (Fig. 12d), there are not enough acceptor states to accommodate all of the electrons in both the shallow and deep donor states. The result is that the shallow donors are partially ionized, and the deep donors are neutral, leading to the dominant emission peaks at 3.25 eV and 3.4 eV. At high Mg concentration (Fig. 12e), both the shallow and deep donors are ionized with enough acceptor states. When an electron is excited to the conduction band by the electron beam in CL, it will first relax to the lowest energy state (i.e., the deep donor state) before radiatively transitioning to the acceptor state, leading to the 2.9 eV emission peak. In short, CL mapping and spot mode CL reveal acceptor deficiency in the sidewall of regrown p-GaN on mesa structures, which is likely due to the lower Mg incorporation efficiency at non-basal planes and faster lateral growth from the sidewall.

Dopant profiling via secondary electrons

Although CL is a useful tool to map out acceptor distributions, some devices may contain p-GaN, UID-GaN, and n-GaN. The spatial dopant distribution in these devices is important for device design, understanding device performance, and failure mechanisms. SIMS is normally used to quantify dopants in semiconductors. However, SIMS has poor lateral resolution, which hinders the development of advanced GaN power devices with complicated *p-i-n* structures. Alugubelli et al. [77] developed an SEM method that used SEs to realize both vertical and lateral dopant profiling in GaN *p-i-n* structures at the sub-micron scale. In an SEM, the incoming electrons are primary electrons (Fig. 13a). The outgoing electrons captured by the SE detector are SEs from the beam-specimen interaction and backscattered electrons (BSEs) stemming from the specimen and from the chamber wall within the solid angle of the detector [107–109]. In addition, there may be current flowing through the specimen (I_{sc}) in order to maintain charge neutrality [110,111]. The relation between these current components in an SEM can be expressed as

$$I_{SE} + I_{BSE} = I_b - I_{sc} \tag{1}$$

where I_{SE} is the SE current, I_{BSE} is the BSE current, and I_b is the primary electron beam current.

When Eq. (1) is divided by I_b on both sides, a relation between SE yield δ (I_{SE}/I_b) and BSE yield η (I_{BSE}/I_b):

$$\delta + \eta = 1 - I_{sc}/I_b \tag{2}$$

For GaN (atomic number of ~38), the BSE yields are not dominant (η less than 0.3) and remain relatively constant with respect to the primary electron beam voltage [112]. The change in electron emission yield is a result of the variation of SE yield with varying primary electron beam voltage. For SE images, an FEI XL 30 FEG microscope was used with an Everhart-Thornley (E-T) SE detector and a short working distance of 3–5 mm to optimize SE collection efficiency. For the measurements of I_{sc}, an FEI Nova NanoLab 200 microscope was used with the primary elec-

Please cite this article in press as: H. Fu et al., Materials Today, (2021), https://doi.org/10.1016/j.mattod.2021.04.011

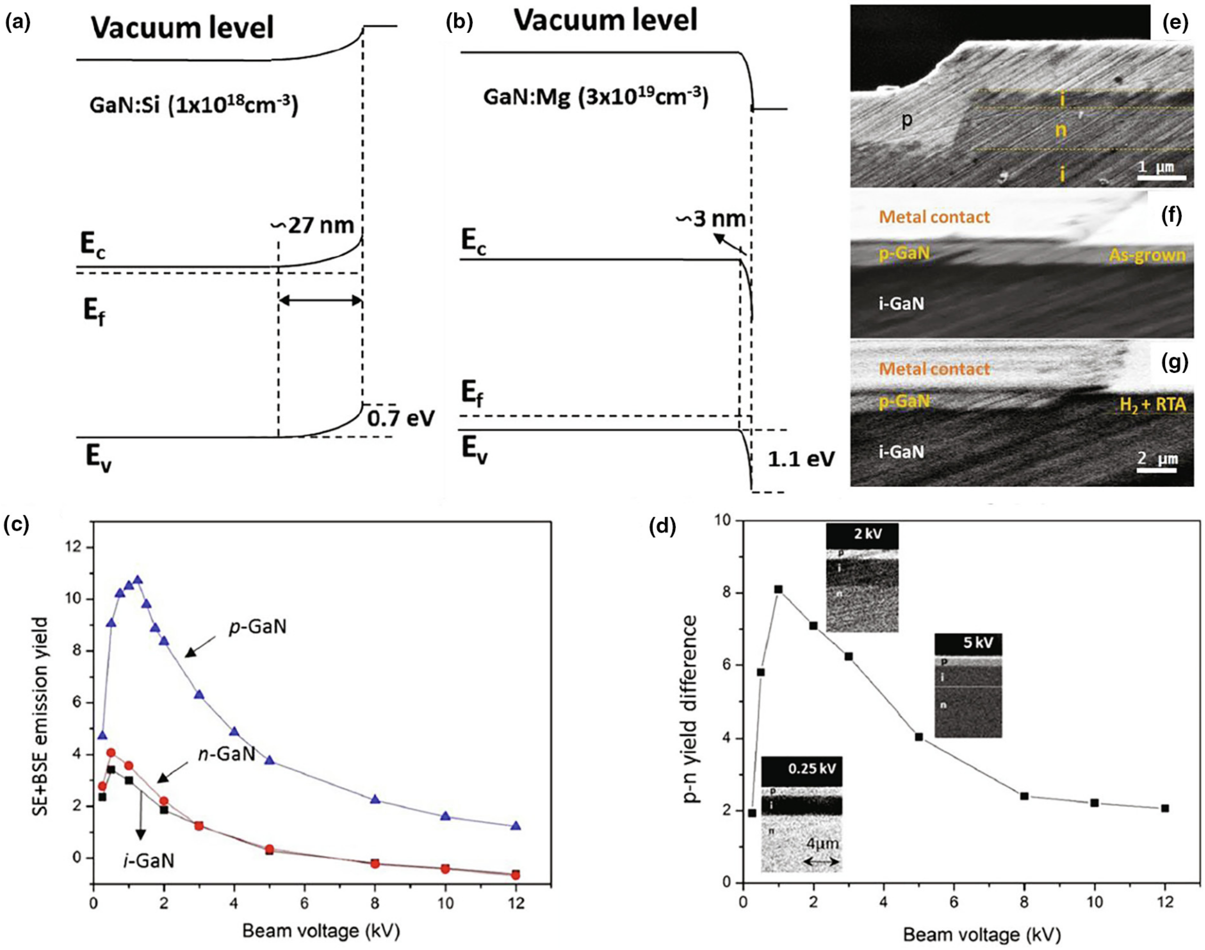

FIGURE 14

Band diagram and band bending near the surface of (a) n-GaN and (b) p-GaN. (c) Electron emission yields as a function of electron beam voltage for p-GaN, i-GaN, and n-GaN. (d) SE yield difference between p-GaN and n-GaN as a function of electron beam voltage. The insets show SE images of GaN *p-i-n* structures at three different beam voltages. SE images of (e) etch-then-regrow *p-i-n* mesa structure, (f) as-grown p-GaN, and (g) hydrogen passivated p-GaN. Reprinted from Ref. [77], with the permission of AIP Publishing.

tron beam voltage varying from 0.25 kV to 12 kV and the beam current in the 30–50 pA range. Fig. 13b shows an SE image of a GaN *p-i-n* structure at 2 kV beam voltage. The emission intensities of the three layers were as follows (Fig. 13c): p-GaN > n-GaN > i-GaN. As a result, the dopant contrast between them was clearly visible so that the three layers can be clearly differentiated.

Alugubelli et al. [77] proposed a mechanism to explain the observed different emission intensities between p-GaN, n-GaN, and i-GaN. Due to the surface states, n-GaN usually exhibits upward band bending near the surface (Fig. 14a), while p-GaN usually has a downward band bending near the surface (Fig. 14b) [113,114]. The upward band bending of the n-GaN surface can deplete electrons from the surface and reduce the SE emission [115,116]. On the contrary, the downward band bending of the p-GaN surface can attract electrons towards the surface and thus increase its SE emission. The lowest SE emission of i-GaN was related to its inability to replenish some SEs due to its lowest conductivity [117]. The incident beam voltage can also impact electron emission yield. Fig. 14c presents the electron yields for p-GaN, n-GaN, and i-GaN. Over the studied beam voltage range, the p-GaN had the highest electron yield, followed by n-GaN and i-GaN. The electron yield of the p-GaN peaked at ~1.25 kV, and those of n-GaN and i-GaN peaked at ~0.5 kV. This trend has been observed in many materials [118] and is due to the relative magnitude of the penetration depth of the primary electrons and the escape depth of the SEs. Before reaching the peak beam voltage, the former is smaller than the latter. With increasing beam voltage, the total number of local SEs increases with excitation volume, which can all be collected by the detectors. After the peak beam voltage is reached, the former is larger than the latter. Most SEs do not have enough energy to reach the surface and are lost inside materials, decreasing electron yields with increasing beam voltage. More importantly, as shown in Fig. 14d, the electron yield difference between p-GaN and n-GaN was the highest for a beam voltage of 1–2 kV. In addition, beyond the beam voltage of 2 kV, the contrast between n-GaN and i-GaN disappeared.

Other factors can also play a role in determining electron emission yields, including doping concentration, surface treatment, beam dwell time, and beam exposure time [77]. It was found that the electron emission yields increased with increasing

Please cite this article in press as: H. Fu et al., Materials Today, (2021), https://doi.org/10.1016/j.mattod.2021.04.011

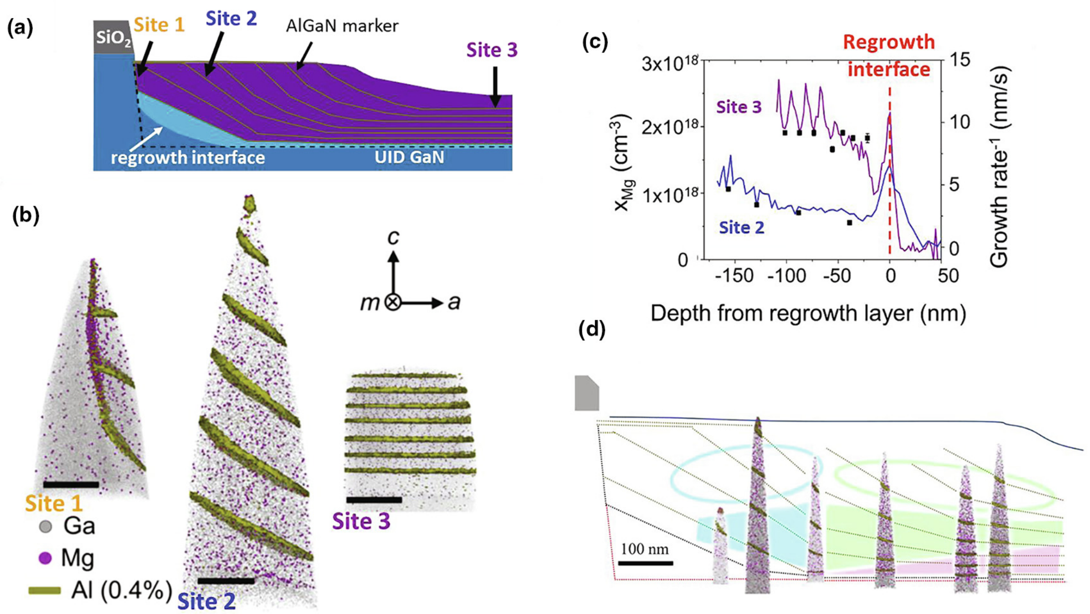

FIGURE 15

(a) Schematic of designed structure for APT analysis with seven Al marker layers. Purple region is Mg-doped. (b) APT reconstructions of regrown p-GaN from three sites. Ga atoms are shown as grey dots, and Mg atoms are shown as purple spheres. Regions in which $x_{Al} > 0.4$ at. % are encapsulated in dark-yellow isosurfaces. (c) Mg concentration (lines) and inverse growth rate (black squares) versus distance from the regrowth interface for trenches along *m*-axis for sites 2 and 3. (d) APT reconstructions of the evolving surface during the non-planar regrowth. Reprinted with permission from Ref. [119]. Copyright (2021) American Chemical Society.

Mg concentrations in p-GaN, which may be used for quantitative dopant profiling of p-GaN. In addition, an oxidized surface can reduce the dopant contrast. Proper surface treatments are critical to observe maximum dopant contrast. In the case of GaN, UV-ozone plus HF treatment worked well. Furthermore, fast scan rates and lower exposure times are also helpful in improving dopant contrast due to the reduced electron beam doses. Using this technique, various lateral and vertical GaN *p-i-n* and *p-n* structures can be imaged, as shown in Fig. 14e–g, which are critical for the development of GaN power electronics.

Atom probe tomography

Regrowth on trench structures is quite challenging, as discussed above. Direct measurements of lateral and vertical doping profiles in non-planar regrown structures can provide a better fundamental understanding of both regrowth processes and device performance. Atom probe tomography (APT) has a sub-nanometer three-dimensional spatial resolution and part-per-million elemental sensitivity. It was implemented to quantitatively analyze the concentration and spatial distribution of Mg atoms in the selective area regrown and selective area doped non-planar p-n junction structure [119]. As shown in Fig. 15a, the designed structure had seven nominally 3 nm thick $Al_{0.06}Ga_{0.94}N$ marker layers (equally spaced in time). Mg was introduced right after the growth of the first marker layer, and six more were inserted during the p-GaN regrowth. The purpose of the Al marker layer was to extract the local growth rate and further reconstruct the evolving shape of the non-planar growth by ex-situ APT analysis. Firstly, atom probes were lifted out from three different locations in the trench, indicated by sites 1 ~3 in Fig. 15b. As indicated by Al markers from sites 1 and 2, semi-polar facets were developed and became the dominant growth front near the edge of the trench, while *c*-plane growth was observed at the center of the trench (site 3). The presence of high Mg concentrations at the dry-etched and regrown interfaces, both on the sidewall and horizontal c-plane surface, indicates the existence of dry etching-induced damage. Mg and Al concentrations in sites 2 and 3 were analyzed and plotted in Fig. 15c. Semi-polar facets in site 2 had about three times faster growth rate compared to the *c*-plane trench center. Intriguingly, a correlation between the Mg dopant concentration and local growth rate was discovered. The Mg concentration is approximately inversely proportional to the growth rate beginning ~20 nm from the regrowth interface. This indicates that the existence of semi-polar facets together with the anisotropy in the growth rate are the origin of non-uniformity in Mg doping of the non-planar regrowth, also observed in [79]. Furthermore, APT was demonstrated to have the capability to qualitatively reconstruct the evolving shape of the growth surface, based on the relative horizontal and vertical positions of the Al marker layers from several atom probes, shown in Fig. 15d.

Regrowth interface

Regrowth interfaces are at the core of ensuring optimal selective area regrowth since the structure and properties of these interfaces affect subsequent regrowth and ultimate device performance. Hence, comprehensive interface characterization is essential for regrowth optimization. In these interface studies, the MOCVD growth was interrupted, the devices were removed from the chamber for etching, and then the samples were re-inserted for a continuation of growth. Different interface etching techniques were investigated. Fig. 16a is a schematic illustrating

Please cite this article in press as: H. Fu et al., Materials Today, (2021), https://doi.org/10.1016/j.mattod.2021.04.011

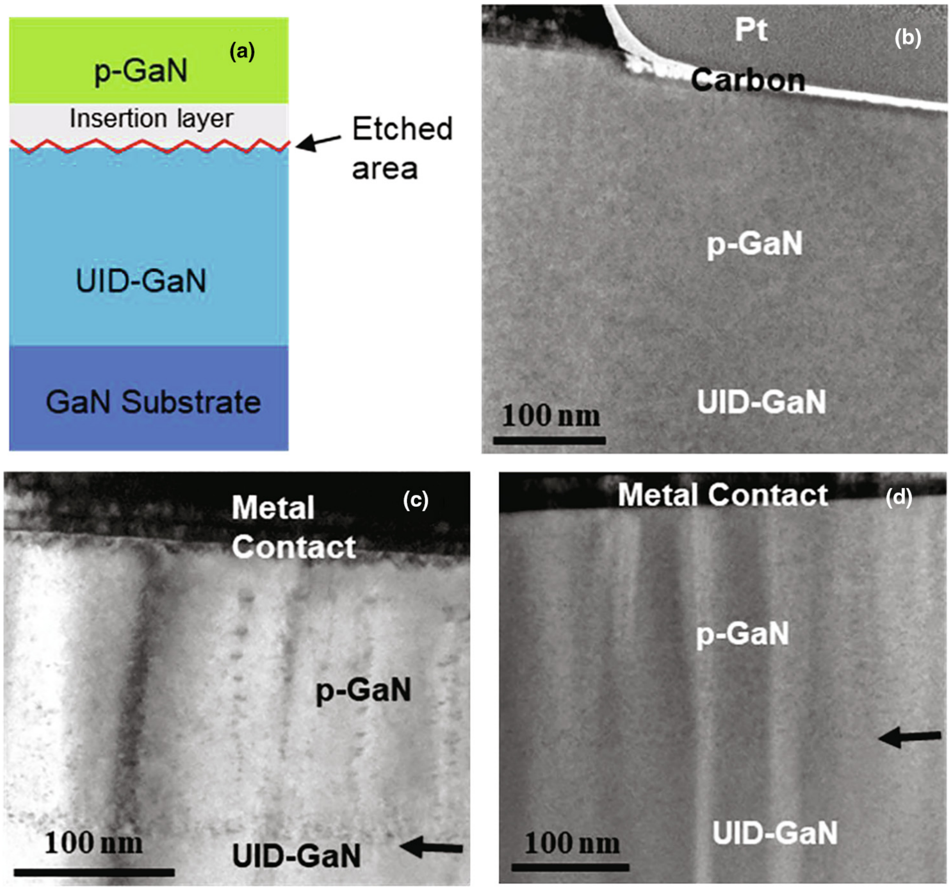

FIGURE 16

(a) Schematic of regrown GaN p-n junctions. TEM cross-section images of (b) as-grown sample, (c) etched sample with a high etching rate, and (d) etched sample with a low etching rate. Reprinted with permission from Ref. [120]. Springer Nature, Copyright © 2021, The Minerals, Metals & Materials Society.

the device geometry used for these studies. As a reference, a sample was grown epitaxially without any interruption, and its cross-section TEM image is shown in Fig. 16b [120]. No etching defects are visible, and the precise location of the interface cannot be determined. Fig. 16c shows the cross-section TEM image of a sample under fast etching [120]. The interface (marked with an arrow) between the p-GaN and UID GaN is clearly visible, and precipitates can be observed within the p-GaN layer and along the visible interface. This device had a reverse bias breakdown voltage of 600 V. Fig. 16d shows the cross-section TEM image of a sample under slow etching [120]. No evidence of precipitates or etching damage is visible. This device had the lowest leakage current of the tested devices, and it is notable that the breakdown voltage had doubled to 1.2 kV, even though the device was subjected to the same growth conditions as the devices shown earlier in Fig. 16b and c. It can be seen that the device performance is closely related to the regrowth interface, which is characterized by *C*–*V*, SIMS, TEM, and SPM in the following discussions.

C–*V* measurements are commonly used to study the charge distribution in a material [121–124]. Fu et al.[68] observed frequency dispersion in the capacitance of regrown GaN p-n junctions. This result indicates the existence of defects and charges inside the regrown structure. Fig. 17a shows the extracted net charge distribution in the regrown p-n junction. A very high donor charge concentration on the order of 10^{17}-10^{20} cm^{-3} occurs within 100 nm from the regrowth interface. Furthermore, another regrown p-n junction with 275 nm UID-GaN insertion layer between the n-GaN and regrown p-GaN had a completely different net charge distribution. The high charge concentrations moved to ~300 nm, where the regrowth interface was located. The charge concentration was much lower near the regrown p-GaN due to the UID-GaN insertion layer. The origin of these charges at the regrowth interface was further investigated by SIMS. Fig. 17b presents the SIMS profile of the regrown p-n junctions [68]. An accumulation of impurities at the regrowth interface was observed, including a large amount of Si, some O, and some C. The O may come from the atmosphere, and C is likely due to the metalorganic sources and/or reactor chambers. The source of Si is still not clear and under investigation. These Si and O impurities contributed to the high density of donor charges at the regrowth interface. Stricklin et al. [125] investigated the interfacial impurity incorporation on regrown *m*-plane p-n junctions with various growth interruptions. They found that the concentrations of Si and O impurities increased for the following growth interruptions: (from low to high) chamber for 10 min, loadlock for 10 min, outside for 10 min, and outside for a week. The mechanism behind this trend is still under

Please cite this article in press as: H. Fu et al., Materials Today, (2021), https://doi.org/10.1016/j.mattod.2021.04.011

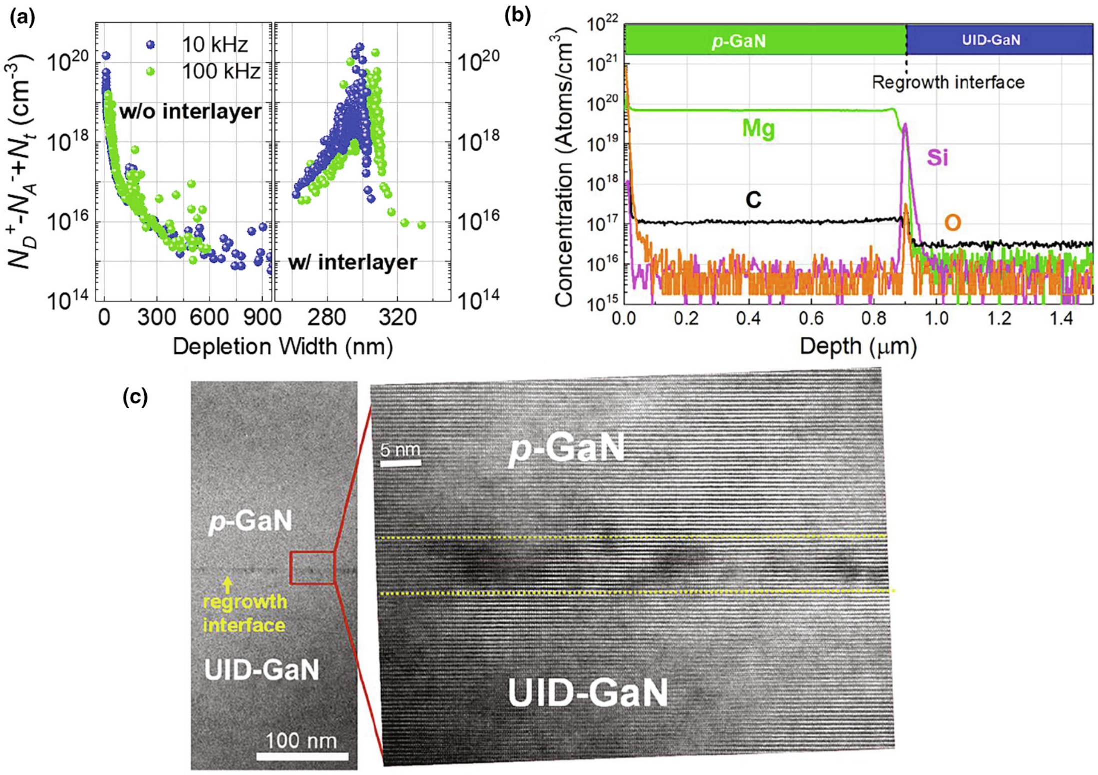

FIGURE 17

(a) Net charge distribution profile for GaN regrown p-n junctions without an insertion layer and with an UID-GaN insertion layer. The depletion depth starts from the end of the regrown p-GaN. N_D^+ is ionized donor concentration, N_A^- is ionized acceptor concentration, and N_t is the charged trap concentration. (b) SIMS profile of the regrown p-n junctions. (c) TEM images of regrown p-n junctions with the regrowth interface clearly invisible. Reprinted from Ref. [68], with the permission of AIP Publishing.

investigation. However, it is clear that it is preferable to keep growth interruptions to a minimum to reduce interfacial impurities.

Furthermore, the TEM image in Fig. 17c directly shows the regrowth interface and the disordered interfacial layer. The large donor-like impurities at the regrowth interface made the interface behave like a thin n$^+$-GaN layer. It may form a tunneling diode with the regrown p-GaN, which is consistent with the observed tunneling-dominated reverse leakage current [68]. In addition, these charges at the regrowth interface increased the local electrical field, resulting in increased reverse leakage and premature breakdown, which is one of the biggest challenges facing selective area regrowth. Methods to mitigate this problem are discussed later in Section 4. Other phenomena related to the regrowth interface, such as resistive switching [126], were also observed.

Electron holography

Electron holography is a valuable tool to investigate how charges at the regrowth interface impact electrostatic potential energy profiles [127]. These may provide some insight into the high leakage currents in regrown p-n junctions. Electron holography is an interferometric TEM technique able to quantify the phase shifts of the electron wave within the studied material, where the phase shift is proportional to a product of electrostatic potential energy and the sample thickness. Alugubelli et al. [128] carried out electron holography studies for continuously grown and regrown GaN *p-i-n* structures in an FEI Titan TEM at a beam voltage of 300 kV. In the continuously grown *p-i-n* structure, the potential profile in the i-GaN layer showed a straight line with a uniform slope. Two regrown GaN *p-i-n* structures were investigated: one without the insertion layer (Fig. 18a and b) and one with a thin insertion layer (Fig. 18c and d).

For the structure without the insertion layer (Fig. 18a), there was upward curvature on the p-GaN side of the regrowth interface and downward curvature on the i-GaN or n-GaN side of the regrowth interface. According to Poisson's equation, it was estimated that charges with a density of $\sim \sim 10^{19}$ cm^{-3} accumulated on each side of the regrowth interface. In SIMS analysis of the same structure (Fig. 18b), three impurity peaks overlapped at the regrowth interface: Mg, Si, and O with peak concentrations of $\sim 2 \times 10^{19}$ cm^{-3}, $\sim 3 \times 10^{19}$ cm^{-3}, and $\sim 3 \times 10^{17}$ cm^{-3}, respectively. It is also interesting to note that a local maximum in the Mg concentration was observed in the SIMS profile, indicating Mg gettering. This is likely due to the often observed Mg precipitates in cross-sectional TEM images of highly doped p-GaN. The high concentrations of Si at the regrowth interface may also affect Mg gettering and precipitates. The presence of these impurities can explain the potential profile curvature near the regrowth interface in Fig. 18a. The downward curvature was due to donor charges from Si and O. The upward curvature was likely caused by high hole concentrations resulting from the

Please cite this article in press as: H. Fu et al., Materials Today, (2021), https://doi.org/10.1016/j.mattod.2021.04.011

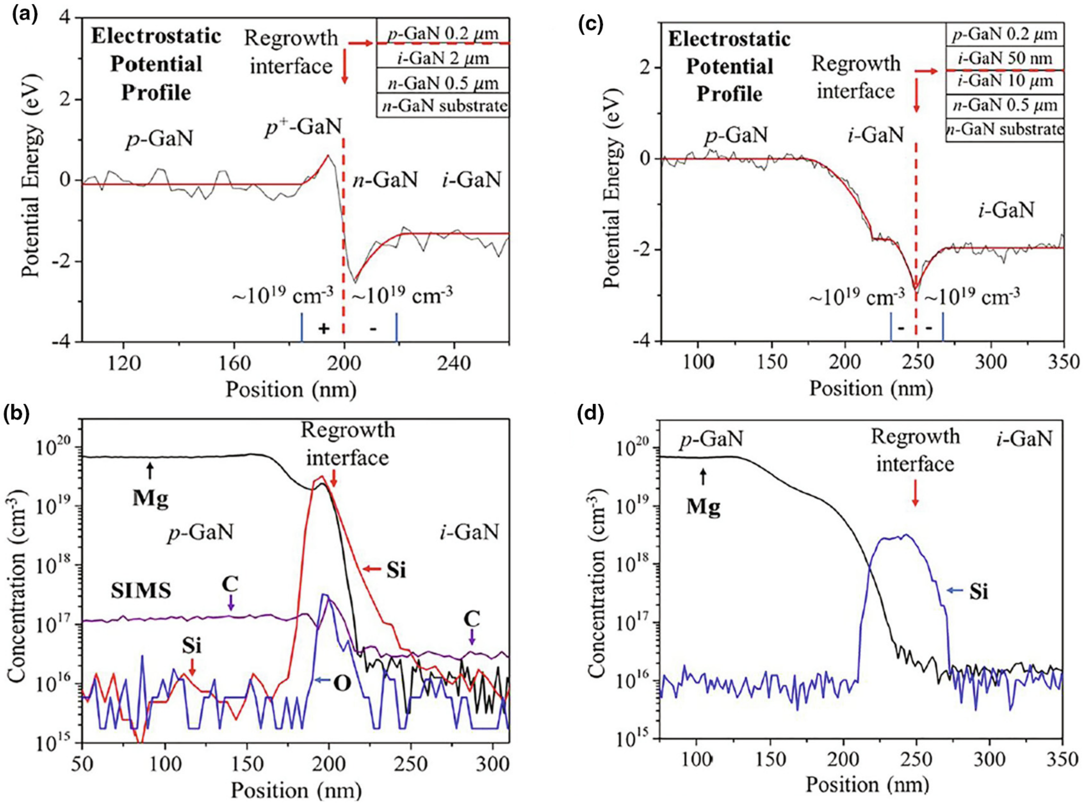

FIGURE 18

(a) Electrostatic potential profile of the p-i interface in a regrown GaN p-i-n structure (as shown in the inset) obtained by electron holography. The charge densities near the regrowth interface are also indicated. (b) SIMS profile of the regrowth interface in (a). (c) The electrostatic potential profile of the regrown GaN *p-i-n* structure with a 50 nm undoped GaN insertion layer. The inset shows the GaN epitaxial structure. (d) SIMS profile of the regrowth interface in (c). The broadening of the signals at the regrowth interface is an artifact due to the SIMS sputtering process. Reprinted from Ref. [128], with the permission of AIP Publishing.

co-doping of Mg with Si and or O. It has been observed that Mg/Si or Mg/O co-doping can significantly enhance hole concentrations by up to two orders of magnitude [129]. This effect is attributed to the lower ionization energies of the formed acceptor–donor-acceptor complexes. A doping profile study on GaN tunneling junctions also showed the overlap of Mg and Si at the interface [130]. Thus, it is hypothesized that the regrowth interface may behave like a p^{+}-n^{+} tunneling junction, resulting in larger leakage currents.

For the structure with the insertion layer (Fig. 18c), the measured potential profile was different. A dip was observed, indicating a positive sheet charge that was surrounded by negatively charged regions. Based on the curvature of the potential profile at the regrowth interface, the charge was also estimated to be $\sim 10^{19}$ cm^{-3}. The SIMS analysis in Fig. 18d shows that the insertion layer moved the Si peak away from Mg, which is consistent with the *C*–*V* measurements. Thus, there was no upward curvature at the p-GaN side due to the co-doping mechanism, and thus no formation of p^{+}-n^{+} tunneling junction at the regrowth interface. As discussed in detail in Section 5, this structure with a thin insertion layer exhibited much lower leakage currents. These results also show that the etching process is critical in affecting the impurities and charges at the regrowth interface.

Scanning probe microscopy

Scanning probe microscopy (SPM) measurements – including but not limited to atomic force microscopy (AFM), scanning Kelvin probe force microscopy (SKPM), and scanning capacitance microscopy (SCM) – are uniquely suited to providing information about both structural morphology and electronic properties of semiconductor epitaxial layers and device structures with a spatial resolution on the order of ~1–100 nm. For epitaxially grown or regrown interfaces, SPM measurements performed in the cross-sectional geometry enable characterization of the electronic properties of buried interfaces that can directly impact device performance. [131–133] The availability of GaN substrates for homoepitaxial growth enables cleaving to produce extremely flat exposed cross-sections of epitaxial layers and devices for SPM characterization – a key requirement for obtaining high-quality measurements of electronic properties by techniques such as SKPM and SCM [134,135].

Fig. 19a shows a schematic illustration of MOCVD-grown GaN p-n junctions, with the junction interface either grown without interruption (as-grown) or regrown after dry etching of the UID-GaN layer (regrown), along with the tip-sample geometry and cross-sectional imaging area employed in the characterization of a cleaved cross-sectional surface by SKPM. Fig. 19b

Please cite this article in press as: H. Fu et al., Materials Today, (2021), https://doi.org/10.1016/j.mattod.2021.04.011

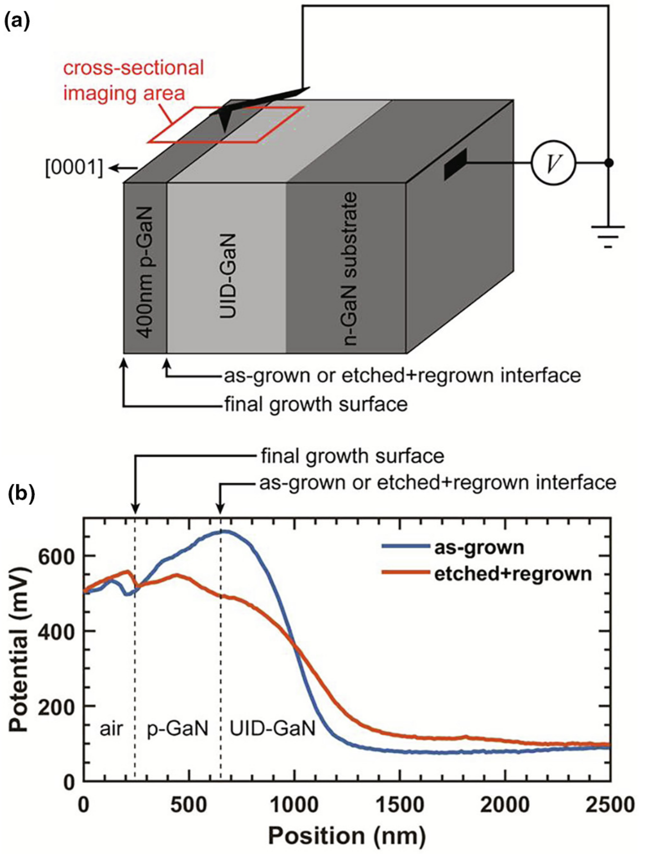

FIGURE 19

(a) Schematic of MOCVD-grown GaN p-n junctions, with the junction interface either grown without interruption (as-grown) or regrown after dry etching of the UID-GaN layer (regrown), along with the tip-sample geometry and cross-sectional imaging area employed in the characterization of a cleaved cross-sectional surface by SKPM. (b) Line plot of potential measured for each type of sample, averaged over a distance of 500 nm parallel to the p-n junction interface.

shows line plots of the potential measured for each type of sample, averaged over a distance of 500 nm parallel to the p-n junction interface. As shown in Fig. 19b, there was a clear transition in potential at the p-n junction interface for both types of structures. The depletion region was located predominantly in the UID-GaN region, as expected due to the lower dopant concentration (lightly n-type) in that region compared to that in the p-type GaN layer. The total potential difference measured across the p-n junction was smaller than the expected built-in potential, which is attributed to partial Fermi-level pinning at the cleaved cross-sectional surface. The depletion layer width estimated from these measurements for the as-grown junction, approximately 650 nm, suggests a background donor concentration in the UID-GaN layer of $\sim 7 \times 10^{15}$ cm^{-3}. Two additional features are of note. First, the potential in the p-type GaN region of the regrown sample was significantly lower than that of the as-grown sample. This observation is consistent with SIMS measurements on similarly regrown samples, as shown in Fig. 17 and Fig. 18, that reveal the presence of a narrow, heavily Si-doped layer at the regrown interface. Such a layer would reduce the effective hole concentration at that location, consistent with the observed reduction in potential in the regrown junction sample. Second, the depletion layer width was substantially greater in the regrown structure than in the as-grown structure, with the deviation between the potentials of the as-grown and regrown samples extending to ~1500 nm below the regrown p-n junction interface. This observation indicates that defects are present in the UID-GaN region below the regrown interface, up to a distance of ~1500 nm below the interface. Such defects might be expected due to subsurface damage occurring during the etch process and could significantly influence device characteristics such as ideality factor and leakage current in p-n junction diodes. Studies of such correlations are currently underway, with SKPM and related techniques providing unique sensitivity to defects present at low concentrations – sufficient to strongly influence device behavior, but too low or of a nature that renders them challenging to observe by other techniques.

Etching technologies

Etching is a key step in selective area regrowth. ICP dry etching is one of the most used etching techniques for GaN devices. In the above, it was shown that ICP dry etching is not ideal for regrowth surfaces since it can result in impurities, charges, interfacial states, and disordered atomic arrangements at the regrowth interface. Previous reports have also demonstrated that ICP etching can result in non-stoichiometric surfaces in GaN and deep defect levels on etched GaN surfaces [136–138]. In this section, three novel etching techniques to alleviate the regrowth issues caused by traditional ICP dry etching or even replace ICP etching, are presented, including low-power dry etching, photoelectrochemical (PEC) wet etching, atomic layer etching, and *in situ* and selective area etching.

Low-power dry etching

One of the most critical issues in GaN selective area regrowth is the high reverse leakage current in the regrown p-n junction. There are two contributors to this problem: (1) impurities and contamination at the regrowth interface such as Si, O, and C, as revealed by the SIMS results [68]; (2) ICP dry etching damage. Therefore, it is vital to investigate the effects of surface treatment and ICP etching on the electrical properties of regrown p-n junctions. Planar regrown p-n junctions were used as a test vehicle to obtain essential knowledge about the etch-then-regrowth process. The device structure is shown in Ref. [139]. It should be noted that the hydrogen-plasma treated region served as the edge termination; more details of this hydrogen-plasma treatment can be found elsewhere [36,38].

Two samples (UID-GaN on GaN substrates) were co-loaded into the MOCVD reactor for p-GaN regrowth without any surface treatment. One of the samples was without ICP etching, and the other sample was with ICP etching at a power of 70 W. The ICP power of 70 W resulted in an etching rate of 200–300 nm/min, a reasonable value for GaN device fabrication. However, both samples suffered from high reverse leakage current. This result indicates that both non-etched and etched surfaces are not optimal for regrowth [139]. The two samples were then treated with UV-ozone and HF and HCl acid treatments prior to the regrowth. The UV-ozone treatment can oxidize the

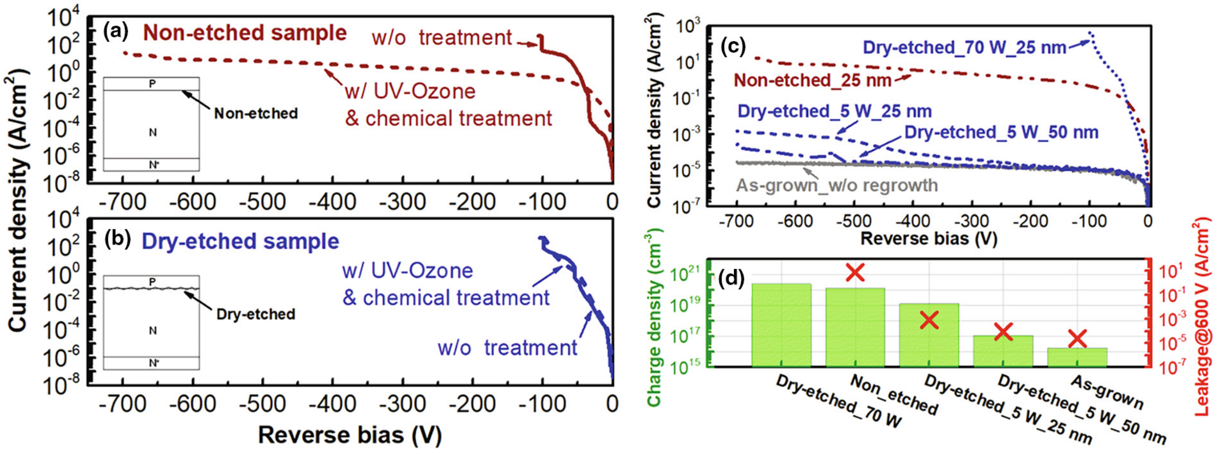

FIGURE 20

Reverse *I–V* characteristics of (a) non-etched and (b) etched samples with or without surface treatments. (c) Reverse *I–V* characteristics of the non-etched sample and different etched samples. The as-grown sample is also shown as a reference. All the etched samples were treated with UV-ozone, HF, and HCl before the regrowth. The power indicates the ICP etching power, and the thickness indicates the insertion layer thickness. (d) Charge density at the regrowth interface (histogram) and leakage current (cross mark) at −600 V for the five samples in (c). © [2019] IEEE. Reprinted with permission from Ref. [139].

surface and any organic residue contaminant, and the acids can remove oxidized materials and further clean the surface. It is also interesting that Pickrell et al. [140] showed that dilute KOH was a useful post-etching surface treatment method, even though the etching damage was not completely removed. The non-etched sample showed a significant reduction in the reverse leakage current (Fig. 20a). However, the etched sample had little improvement (Fig. 20b). It is hypothesized that the etching damage in the etched sample was too severe to be recovered by any surface treatment.

In order to confirm this hypothesis, a much lower ICP etching power of 5 W (etching rate of ~20 nm/min) was used for the ICP dry etching. As shown in Fig. 20c, the leakage current was reduced by over 4–5 orders of magnitude [139]. It should also be noted that the insertion layer is also beneficial for decreasing the leakage current. This is because the insertion layer can shift the junction away from the regrowth interface, preventing the formation of p^+-n^+ tunneling junctions, which is consistent with the previous discussion [128]. The thickness of the insertion layer must be optimized since a too thin insertion layer is not effective, and a too thick insertion layer is not practical. Fig. 20d compares the charge concentrations at the regrowth interfaces and reverse leakage currents of the samples in Fig. 20c. The higher the charge concentration at the regrowth interface, the larger the reverse leakage current. The regrown samples had large concentration peaks on the order of 10^{17}-10^{20} cm^{-3} at the regrowth interface, while the as-grown sample showed a low and uniform charge distribution on the order of ~10^{16} cm^{-3}. These large amounts of charges at the regrowth interface can induce a larger electric field and a thinner effective barrier that facilitates carrier tunneling and increases leakage current [139]. The etched sample with the 5 W ICP etching and the 50-nm insertion layer showed very low interfacial charge density and reverse leakage current, which is comparable to that of the as-grown sample. These results indicate that low-power ICP etching combined with proper surface treatment can not only reduce dry etching damage but also remove the interfacial charges, both of which are highly beneficial for selective area regrowth [139].

Photoelectrochemical etching

A comprehensive study was carried out [141] to evaluate the effect of photoelectrochemical (PEC) wet etching on deep-level defects in regrown vertical GaN Schottky diode via steady-state photocapacitance (SSPC). This technique utilizes sub-bandgap-energy light to excite photoemission of carriers that are trapped in the deep-level defect states in the depletion region of a diode. The carriers are then swept out of the junction, and the remnant excess space charges reduce the depletion region width, leading to an additional depletion capacitance, i.e., the photocapacitance ΔC. When the photon energy of the incident light is close to the energy level of a deep-level defect, the SSPC spectrum will show a threshold, an indicator of a defect.

Five samples were prepared in the study: continuously grown GaN Schottky diode without regrowth as a reference (sample 1), regrown GaN Schottky diode without etching but with solvent isopropanol/de-ionized water (Ace/IPA/DI) cleaning (sample 2), regrown GaN Schottky diode with ICP etching before regrowth (sample 3), regrown GaN Schottky diode with ICP etching and a subsequent AZ400K treatment before regrowth (sample 4), and regrown GaN Schottky diode with ICP etching and a subsequent PEC etching (sample 4). The ICP etching used an ICP power of 130 W and an RF power of 30 W. The PEC etching was performed in a 0.01 M KOH in DI at room temperature with a mercury arc lamp with a surface flux of 100 mW/cm^2. No acid treatments were employed in the experiments. SSPC was carried out on all five samples to study the deep-level defects in the regrown GaN Schottky diodes. A representative SSPC spectrum is shown in Fig. 21a. Three deep-level defects were identified in all samples: $E_c - 1.9$ eV, $E_c - 2.9$ eV, and $E_c - 3.3$ eV, where E_c is the conduction band minimum. The first deep-level defect was likely due to native defects generated by atomic displacement during growth, the second one was related to either C or Ga

Please cite this article in press as: H. Fu et al., Materials Today, (2021), https://doi.org/10.1016/j.mattod.2021.04.011

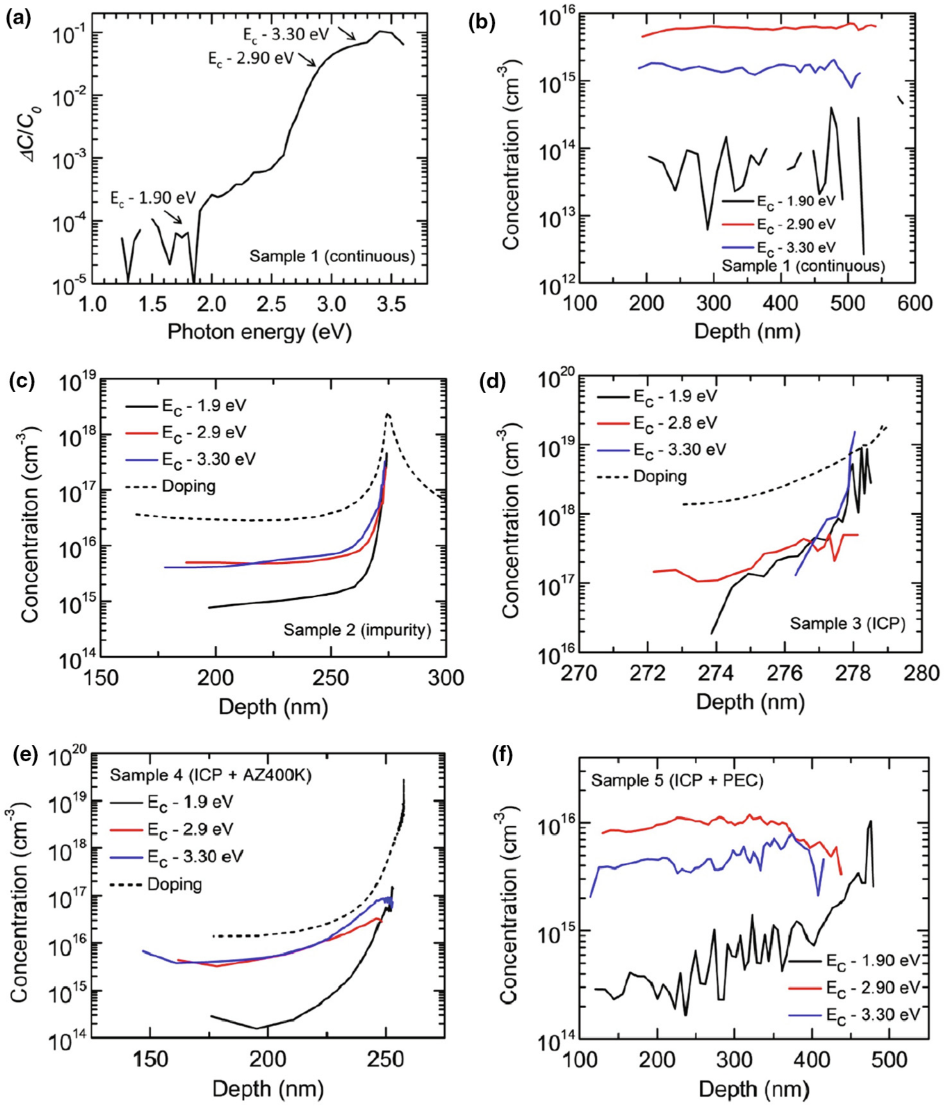

FIGURE 21

(a) Steady-state photocapacitance spectrum of continuously grown vertical GaN Schottky diode without regrowth. Concentrations of deep levels versus depth for (b) continuously grown Schottky diodes (sample 1), (c) regrown Schottky didoes without etching but with solvent cleaning before regrowth (sample 2), (d) ICP etched-and-regrown Schottky diode (sample 3), (e) ICP + AZ400K etched-and-regrown Schottky diode (sample 4), and (f) ICP + PEC etched-and-regrown Schottky diode (sample 5). Reprinted from Ref. [141], with the permission of AIP Publishing.

vacancy or both, and the third one was often associated with C impurities.

Lighted capacitance–voltage (LCV) measurements were also performed to obtain the depth profile of the deep-level defect concentrations. It measures the increase in the apparent doping concentration when the deep-level defects are ionized by light with photon energy close to the energy level of the defects. The profile depths of different samples are different due to the Si and/or O impurities at the regrowth interface, as shown in Fig. 21b–f. Regrown samples 2, 3, and 4 without PEC etching exhibited a large doping spike at the regrowth interface. This also limited the depletion region to the regrowth interface and, therefore, the probing depth. The regrown sample 5 with PEC etching showed no doping spikes at the regrowth interface, similar to the continuous grown sample 1. This indicates that PEC etching is effective in removing the impurities at the regrowth interface. Table 1 summarizes the deep-level defect concentrations above and near the regrowth interface for the five samples. Sample 2 did not show a large increase in the deep-level defect concentrations in the bulk region but did show enhancement of these defects at the regrowth interface (Fig. 21c). Compared with sample 1, ICP etching in sample 3 (Fig. 21d) significantly increased the concentrations of all deep-level defects by several orders of magnitude. The depth profile in Fig. 21d shows tails propagating several hundred nanometers into the bulk region in all defect distributions, indicating these deep-level defects are delocalized. The AZ400K wet treatment was used to mitigate ICP-induced damage because it can etch away surface damaged GaN at a slow rate. Sample 4 showed largely reduced concentrations of three deep-level defects near the regrowth interface. The depth profile of sample 4 (Fig. 21e) still had a tail, which indicates that the ICP-induced damage was not completely recovered. PEC wet etching

Please cite this article in press as: H. Fu et al., Materials Today, (2021), https://doi.org/10.1016/j.mattod.2021.04.011

TABLE 1

Deep-level defect concentrations for samples with different treatments before regrowth. Reprinted from Ref. [141], with the permission of AIP Publishing.

Sample No.	Surface treatment	Above regrowth interface			Near Regrowth interface		
		Ec − 1.9 eV ($\times 10^{14}$ cm^{-3})	(Ec − 2.9 eV) ($\times 10^{14}$ cm^{-3})	(Ec − 3.3 eV) ($\times 10^{14}$ cm^{-3})	(Ec − 1.9 eV) ($\times 10^{14}$ cm^{-3})	(Ec − 2.9 eV) ($\times 10^{14}$ cm^{-3})	(Ec − 3.3 eV) ($\times 10^{14}$ cm^{-3})
1	N/A	1	30	70	N/A	N/A	N/A
2	Ace/IPA/DI	2	20	30	2000	1600	3300
3	ICP (400 nm)	10	200	1000	85 600	5030	81 600
4	ICP (400 nm) + AZ400K	1	30	30	300	300	800
5	ICP (400 nm) + PEC (200 nm)	4	90	30	30	50	70

has a higher GaN etching rate than AZ400K. The concentrations of the deep-level defects were reduced (Fig. 21f) to a level that is similar to those of the continuously grown sample 1. And no tail was observed in the depth profile of Fig. 21f. Due to their different regrowth interface properties, the leakage currents of the five regrown Schottky diodes were compared [141]: sample 1 < sample 5 < sample 4 < sample 3 < sample 2. These results indicate that wet etching such as PEC and AZ400K can help mitigate ICP-induced damage and considerably improve the regrowth interface.

Atomic layer etching

To further improve regrown p-n junctions and related devices, it is critical to tackle the ICP etching damage issues caused by photons, radicals, and ions, which may create defects, impurities, and surface states. We recently demonstrated a novel ALE process for GaN (Fig. 22a). ALE allows controlled material removal using self-limiting chemical processes, thus removing damaged layers without inducing further etching damage. It has a limited ion component, giving the best opportunity to obtain a high-quality interface. Unlike several other materials for which ALE has been developed, direct fluorination of GaN via HF is not a favorable reaction. Therefore, our ALE process began with surface modification via plasma-enhanced atomic layer oxidation to convert the surface to Ga_2O_3. Then, exposure to HF gas reduced the oxide, resulting in GaF_3 at the surface. Trimethylgallium (TMG) or trimethylaluminum (TMA) then underwent ligand exchange with the fluoride surface to produce volatile $GaF(CH_3)_2$, removing the converted surface layer. The ALE of Ga_2O_3 is a fully thermal process and is essential to our GaN etching. These etching methods follow a similar approach to previously reported thermal ALE of Al_2O_3 and TiN [142,143].

The first step of the ALE process was oxidation of the GaN surface, which occurred through O_2 plasma exposure (Fig. 22b). At 100 W RF power, saturation of the oxide thickness was observed at 1.0 nm within 10 s of exposure. The oxide was then reduced by exposure to HF, which resulted in GaF_3 (Fig. 22c). TMA or TMG was introduced to exchange methyl groups at the surface, producing volatile $GaF(CH_3)_2$ and $AlF(CH_3)_2$ (Fig. 22d). Incomplete removal of the surface oxide during HF exposure was observed via X-ray photoelectron spectroscopy (XPS); therefore, several cycles of Ga_2O_3 etching are required after oxidation. Due to the high oxidation rate, multiple exposures of HF and TMG/TMA are required to remove the surface oxide. With three alternating exposures of HF and TMG, oxide deposition was observed via *in situ* ellipsometry due to incomplete removal of the oxide (Fig. 23a). With five alternating exposures of HF and TMG, complete removal of the oxide was observed (Fig. 23b), resulting in an etching rate of ~1.0 nm/supercycle. These results indicate the effectiveness of the ALE process for GaN surfaces, which should be highly useful for the preparation of interfaces prior to regrowth in selective area doping.

In situ and selective area etching

ICP plasma etching is commonly used in the fabrication of GaN devices, but it can cause damage at the surface and subsurface regions. Although methods such as low-power ICP etching, wet etching, and ALE are utilized to alleviate the damage, realizing a defect-free regrowth interface is still challenging. Li et al. [144] developed a vapor-phase etching for GaN in the MOCVD reactor using tertiarybutylchloride (TBCl), i.e., *in situ* etching. It should also be mentioned that H_2 and HCl have also been used for the *in situ* etching of GaN. However, the former leads to rough surfaces due to Ga droplets [145], and the latter is highly corrosive and not suitable for MOCVD [146]. TBCl-based *in situ* etching has proven to be a better choice with faster etching rates, near-equilibrium reaction chemistry, relatively low etching temperatures, and larger etching temperature windows [144].

The experiments were carried out in a horizontal MOCVD reactor, where 1 µm UID-GaN was first grown on sapphire substrates and then etched by TBCl. The *in situ* etching rate on planar GaN was calculated based on thickness measurements done by *in situ* reflectometry [147]. Fig. 24a shows the etching rates as a function of TBCl flow rate at different temperatures with 2000 sccm NH_3 at 200 mbar. The etching rates were higher at higher temperatures, and the etching rate increased linearly with the TBCl flow rate. By extrapolation, at zero TBCl flow rate, the background H_2-related GaN etching rates at different temperatures can be extracted, which are consistent with an independent H_2-etching study over the same temperature range. Assuming that TBCl etching and H_2 etching are independent and concurrent in Fig. 24a, the etching rate of the two processes can be decoupled. The Arrhenius plot is presented in Fig. 24b. The activation energy of H_2 etching was 2.57 eV, while that of TBCl etching was 0.8–0.9 eV at a TBCl flow rate of 10–20 sccm. It is clear that TBCl etching can provide a reasonable etching rate at lower temperatures compared with H_2 etching. The thermodynamics of TBCl etching can be understood as follows [144]. At low

Please cite this article in press as: H. Fu et al., Materials Today, (2021), https://doi.org/10.1016/j.mattod.2021.04.011

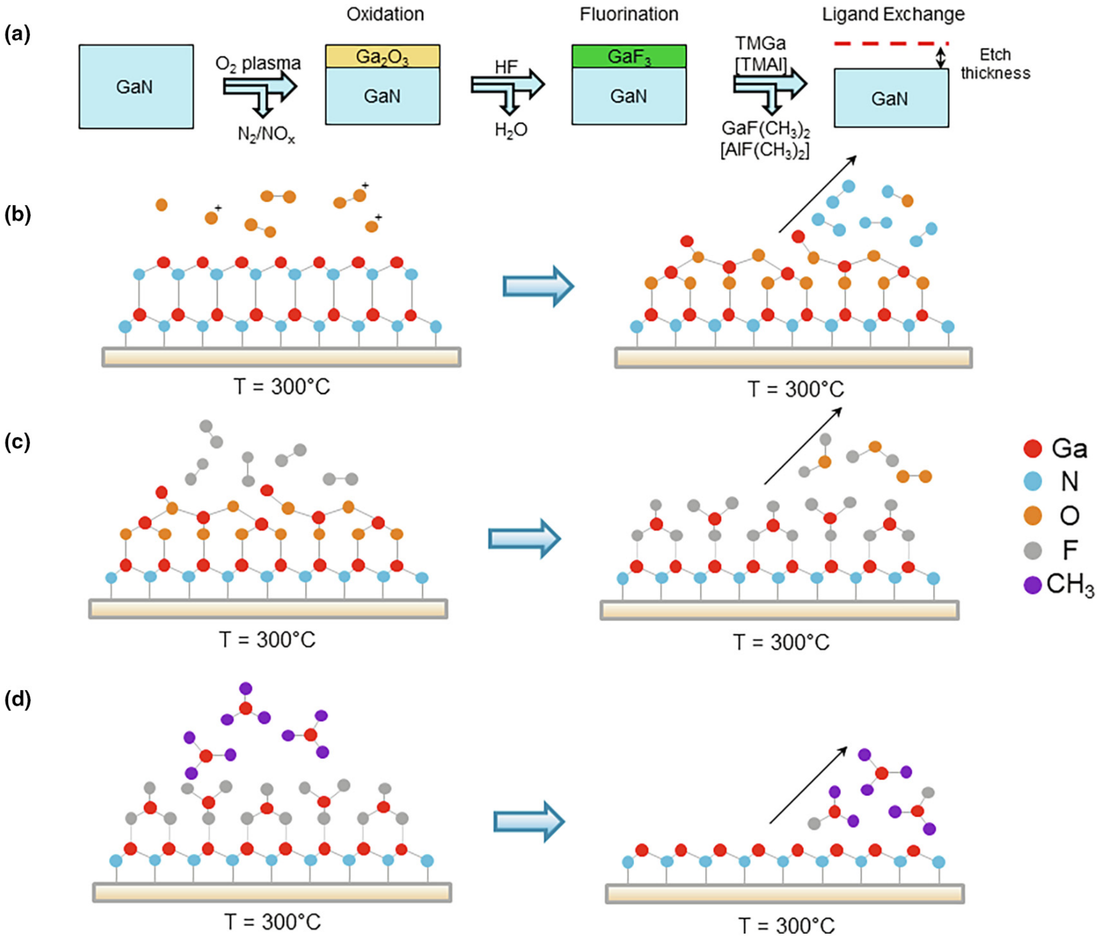

FIGURE 22

(a) Schematics of atomic layer etching processes for GaN. (b)-(c) Schematics of surface reactions during each cycle.

temperatures, the etching is limited by TBCl decomposition [148]. Above the TBCl decomposition temperature of ~550 °C, the etching is limited by the desorption of the byproduct $GaCl_x$. At even higher temperatures, the byproduct can be readily removed, and the etching is in a diffusion-limited regime.

In addition, NH_3 flow rate also plays a critical role in TBCl etching. As shown in Fig. 24c, the etching rate increased with decreasing NH_3 flow rate. At 50 sccm NH_3 flow rate, the etching rate was ~0.5 μm/h at 800 °C, which is ~10 times faster compared with the etching rate at the typical NH_3 flow rate of 2000 sccm. To explain this phenomenon, Li et al. [144] proposed TBCl etching chemistry for GaN. Depending on the availability of reactive H-radicals by NH_3, two different gas-phase reactions can occur. When the NH_3 flow rate is high, and there are abundant H-radicals, TBCl will pyrolyze into $(CH_3)_3C$ and HCl due to the higher binding energy of H–Cl than Cl–Cl [149,150]. When the NH_3 flow rate is low, TBCl will pyrolyze into $(CH_3)_3C$ and Cl radicals [148]. Both HCl and Cl can etch GaN with GaCl byproduct, where Cl-radical etching is faster. Thus, the trend of the etching rate visible in Fig. 24c can be explained as follows. With decreasing NH_3 flow rate, the etching chemistry switched from HCl etching to the faster Cl-radical etching. In addition, low NH_3 partial pressure can also accelerate the $GaCl_x$ desorption. Furthermore, the high etching rate at 50 sccm NH_3 may indicate that the etching is in the diffusion-limited regime.

The developed TBCl etching was further applied to selective area etching on SiO_2 patterned GaN grown on sapphire substrates. Fig. 24d presents the effects of NH_3 flow rate and reactor pressure on the sample morphology after selective area etching. With a high NH_3 flow rate and high reactor pressure (the upper right SEM image), a rough morphology with large pyramids was observed in the trench. This is attributed to the "micromasking effect" due to the low desorption of the etching products [151]. With decreasing NH_3 flow rate and reactor pressure, the surface morphology became smoother with fewer and smaller pyramids. At an NH_3 flow rate of 14 sccm and reactor pressure of 50 mbar, a very smooth trench without pyramids was observed (bottom left SEM image). The cross-sectional SEM image of the trench along [11–20] is shown in the inset of Fig. 24c.

Using the pyramid-free etching condition, TBCl etching was performed on 1.5 μm UID-GaN templates grown on bulk GaN substrates [152]. Four samples with different etching treatments were compared. Sample A was a GaN template without etching. Sample B ~D were GaN templates etched by Cl-based plasma, TBCl, and both Cl-base plasma and TBCl, respectively.

Please cite this article in press as: H. Fu et al., Materials Today, (2021), https://doi.org/10.1016/j.mattod.2021.04.011

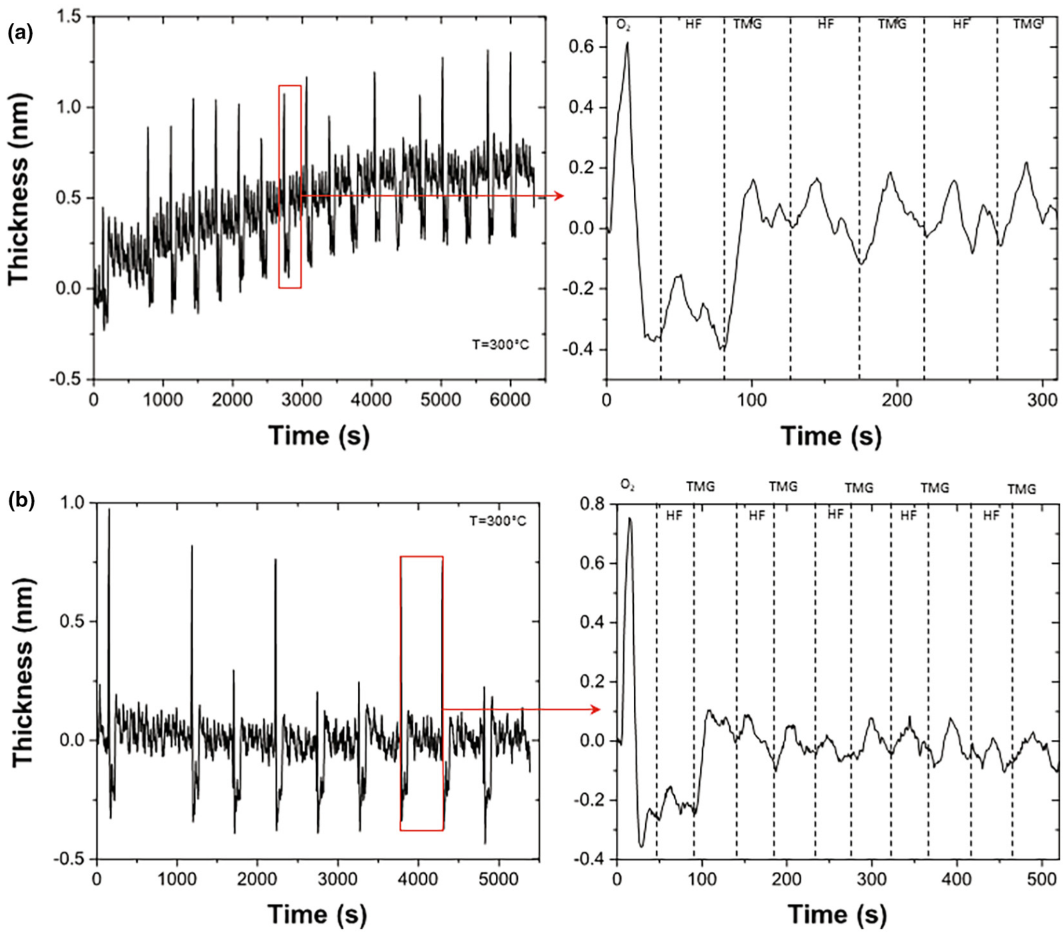

FIGURE 23

Thickness measurements during ALE of GaN using *in situ* ellipsometry for (a) 20 supercycles consisting of 3 alternating exposures of HF and TMG per O_2 plasma, and (b) 10 supercycles consisting of 5 alternating exposures of HF and TMG per O_2 plasma.

The photoluminescence (PL) in Fig. 24e showed strong near-band-edge emissions only from samples A, C, and D, indicating a good surface. These samples either had no etching or TBCl etching. Sample B with only Cl-based plasma etching had an obvious Cl peak from X-ray photoelectron spectroscopy (XPS), as shown in Fig. 24f. Sample D showed no Cl peak due to the TBCl etching after the plasma etching. These results suggest that TBCl etching is able to remove the impurities and damage induced by plasma etching and does not itself introduce damage. These results show that *in situ* TBCl etching can serve as an alternative etching method but without plasma etching damage or help remove the plasma etching damage similar to the ALE. TBCl *in situ* and selective area etching are very promising for selective area regrowth and doping in the fabrication of advanced GaN power electronic devices. Due to the recent development of these novel etching technologies, future work is undergoing to demonstrate high-performance regrown devices using the ALE and TBCl-based *in situ* etching.

Regrown devices

Due to the immature status and the challenges for selective area regrowth, very few regrown devices have so far been reported. In this section, two types of regrown devices are discussed, including GaN p-n diodes and VJFETs. Current regrown p-n diodes are still planar with decent performance. Low-leakage lateral p-n junctions are still under development. Nevertheless, the first normally-off VJFETs with regrown p-GaN gate were demonstrated, although leakage currents and breakdown voltages need further improvement.

p-n diodes

Regrown p-n junctions are the cornerstone of selective area growth and doping. Although high performance lateral p-n junctions are still under development, several vertical regrown p-n junctions have been demonstrated. Hu et al. [91] reported a 1.1-kV vertical GaN regrown p-n diode without ICP dry etching where the p-GaN regrowth was completed using molecular beam epitaxy (MBE). The n-GaN drift layer was grown by MOCVD with a thickness of 8 μm and a Si concentration of $\sim 2 \times 10^{16}$ cm^{-3}. The device had a specific on-resistance of 3.9 $m\Omega \cdot cm^2$, a turn-on voltage of 3.9 V, an on/off ratio of $\sim 10^{11}$, and an ideality factor of 2.5. Compared with the as-grown device with the same structure, the regrown device showed high specific on-resistance and recombination currents due to the regrowth interface. The large reverse leakage current in the regrown device was attributed to defect-assisted hopping conduction in the regrown p-GaN and/or at the regrowth interface.

Please cite this article in press as: H. Fu et al., Materials Today, (2021), https://doi.org/10.1016/j.mattod.2021.04.011

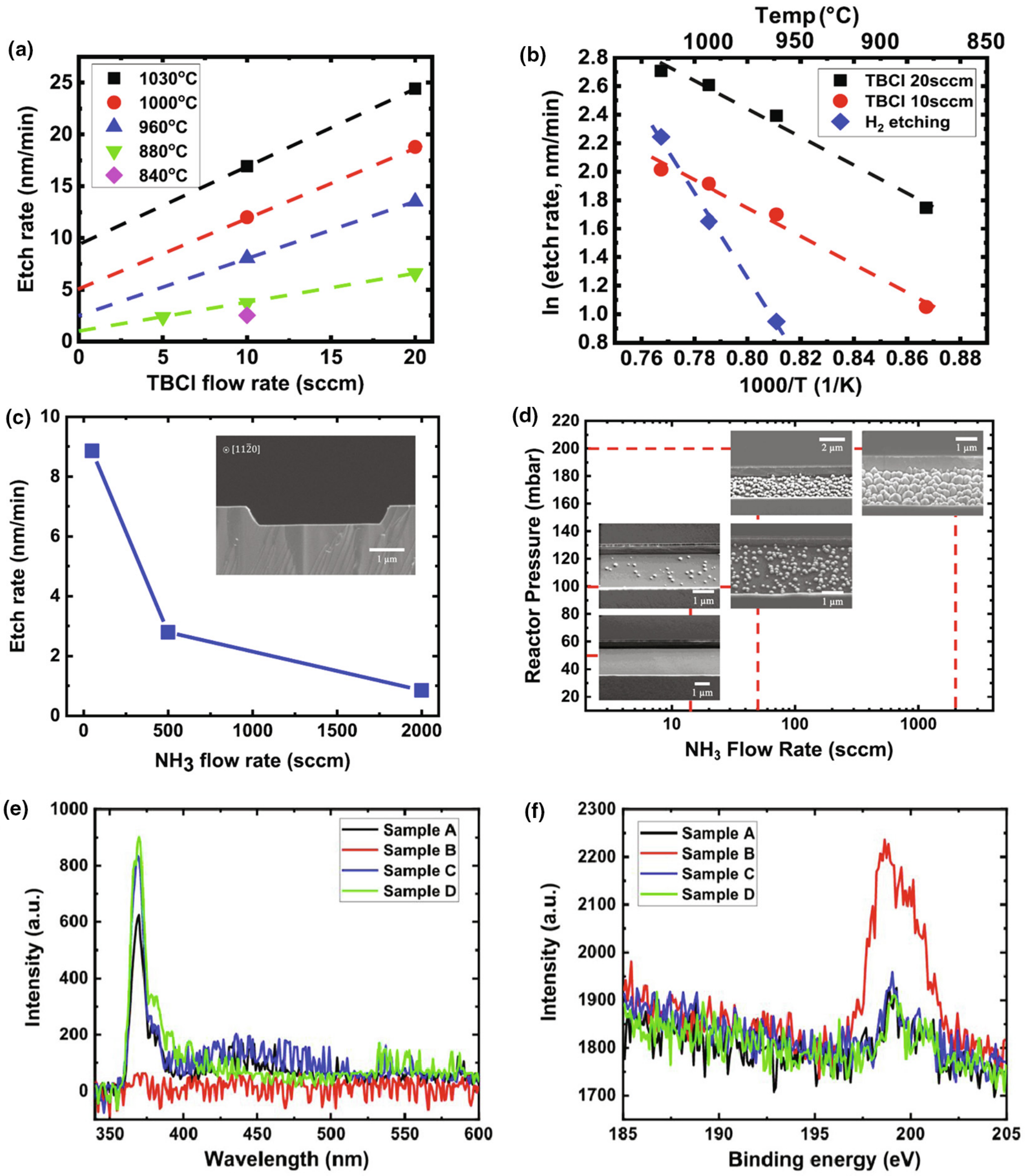

FIGURE 24

(a) GaN planar etching rate as a function of TBCl flow rate using hydrogen as carrier gas. (b) Arrhenius plot of the GaN planar etching rate in different TBCl flow rates: 20 sccm, 10 sccm, and 0 sccm (i.e., H_2 etching). (c) GaN planar etching rate as a function of NH_3 flow rate with 5 sccm of TBCl using hydrogen as the carrier gas. The inset shows the cross-sectional SEM image of stripe patterns along [11–20] using SiO_2 masks. (d) SEM images of selective area etching with different NH_3 flow rates. (e) PL and (f) XPS of Cl 2p spectra on Sample A∼D with different etching treatments. (a)–(d): Reprinted from Ref. [144], with the permission of AIP Publishing. (e) an d(f): Reprinted from Ref. [152], Copyright (2020), with permission from Elsevier.

For the purpose of mass production, p-GaN regrowth by MOCVD is highly preferred. To mimic the process of selective area regrowth, ICP dry etching was performed prior to the regrowth. Fu et al. [139] demonstrated high performance MOCVD regrown GaN p-n junctions with the highest breakdown voltages of ∼1.3 kV with a novel multi-step ICP etching (Fig. 25a and b). As discussed above, low-power ICP dry etching can improve the reverse leakage characteristics of the regrown p-n junctions. However, the low etching rate of the low-power ICP etching is not always practical and can be time-consuming for device structures with deep trenches and mesas. To solve this problem, a multi-step etching was developed with decreasing ICP etching powers from 70 W to 35 W to 5 W to 2 W. This etching strategy can not only provide decent etching rates but also largely alleviate the etching damage and result in good regrowth surfaces [139]. The device showed a specific on-resistance of 0.8 mΩ·cm^2, an on/off ratio of 10^{10}, and an ideality factor of ∼2, which are close to values for the as-grown samples. In addition, Yamada et al. [153] showed that a subsequent thermal annealing step after low-power ICP etching could further improve device performance. This is likely due to the removal of incomplete reaction products (e.g., $GaCl_x$) remaining on the surface after the low-power ICP etching [154,155] and improved surface roughness.

Please cite this article in press as: H. Fu et al., Materials Today, (2021), https://doi.org/10.1016/j.mattod.2021.04.011

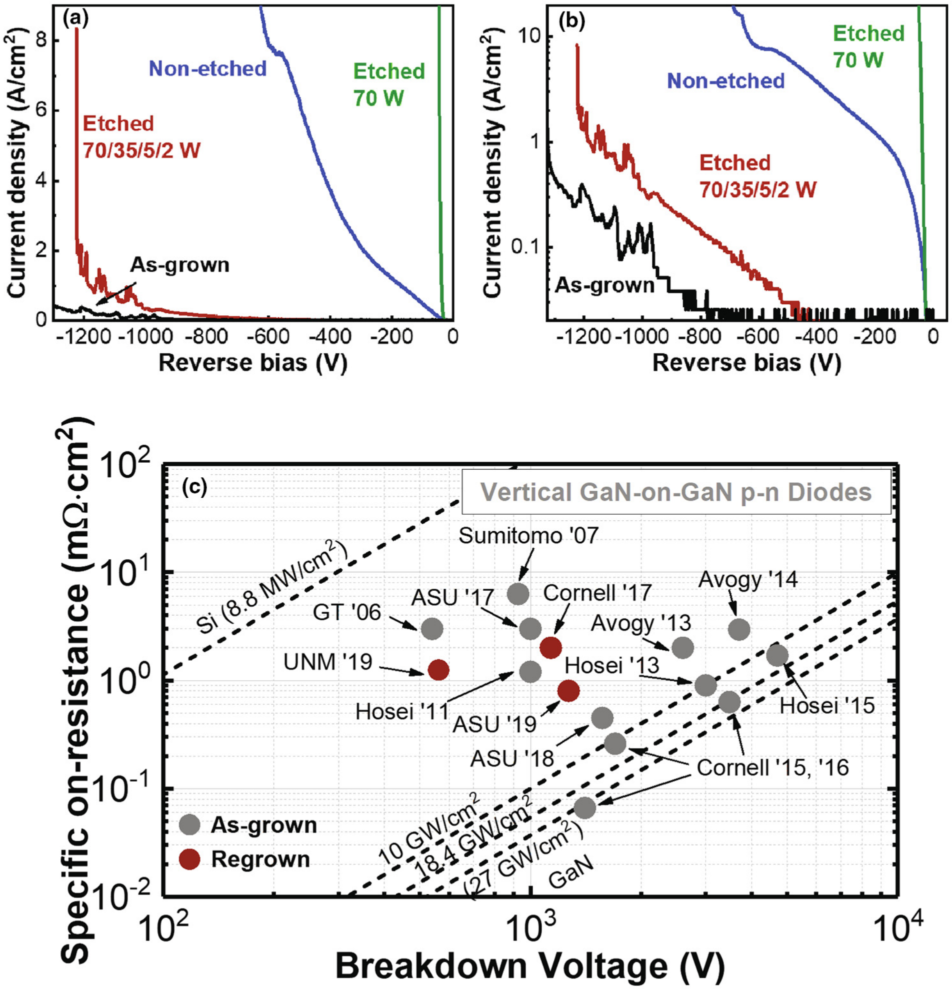

FIGURE 25

Reverse *I–V* characteristics of as-grown non-etched sample, sample with single-step etching, and sample with multi-step etching in (a) linear scale, and (b) semi-log scale. The devices were measured by Tektronix 370A curve tracer, and the leakage current measurements are limited by the relatively low current resolution of the setup. (c) Benchmark plot of specific on-resistance versus breakdown voltages for reported as-grown and regrown GaN-on-GaN vertical p-n diodes. All values of specific on-resistance are as-reported values and normalized by the area of p-contact. © [2019] IEEE. Reprinted with permission from Ref. [139].

For selective area regrowth in trenches, the regrowth interfaces contain both c-plane and nonpolar *m*- or *a*-plane. These two types of crystal planes possess very different material properties. For example, nonpolar planes have a larger tendency to incorporate impurities than *c*-plane. Aragon et al. [73] further revealed that when the impurity concentration is moderate ($<5 \times 10^{17}$ cm^{-3}), the forward and reverse characteristics of *m*-plane p-n diodes were not significantly degraded. When the impurity concentration was high, different impurities showed different impacts. High C levels did not increase the reverse leakage current by much, while high Si and O levels led to very large reverse leakage currents. Monavarian et al. [69] showed a regrown nonpolar *m*-plane p-n junction without dry etching. The device showed a breakdown voltage of 540 V, a specific on-resistance of 1.7 mΩ·cm^2, a turn-on voltage of ~3 V, an on/off ratio of 10^9, and an ideality factor of 1.7. Fig. 25c presents the benchmark plot for the as-grown and regrown vertical GaN-on-GaN p-n diodes [139]. The Baliga's figure of merit of the regrown p-n diodes by Fu et al. [139] was 2.0 GW/cm^2, which is among the best performance in regrown devices and even comparable to some of the as-grown devices. The performance of GaN regrown p-n junctions is expected to approach the GaN material limit with further improvements in the etching technology, surface treatment, and device fabrication.

Vertical junction field-effect transistors

GaN VJFETs were first proposed by Kizilyalli et al. [156], and Ji et al. [157] performed device simulations and optimization. Kotzea et al. [158] showed GaN VJFETs on sapphire substrates with a low on/off ratio (less than 2) by selective area regrowth. However, high performance GaN VJFETs have not been experimentally demonstrated on bulk GaN substrates. Based on the study of selective area regrowth discussed above and a self-planarization process, Yang et al. [159] reported the first experimental demonstration of decent GaN VJFETs with a high on/off ratio of ~100. The detailed fabrication process is shown in Fig. 26. Each VJFET under test consisted of six fins with a length of 160 μm and a width of 1 μm. The current density was normal-

Please cite this article in press as: H. Fu et al., Materials Today, (2021), https://doi.org/10.1016/j.mattod.2021.04.011

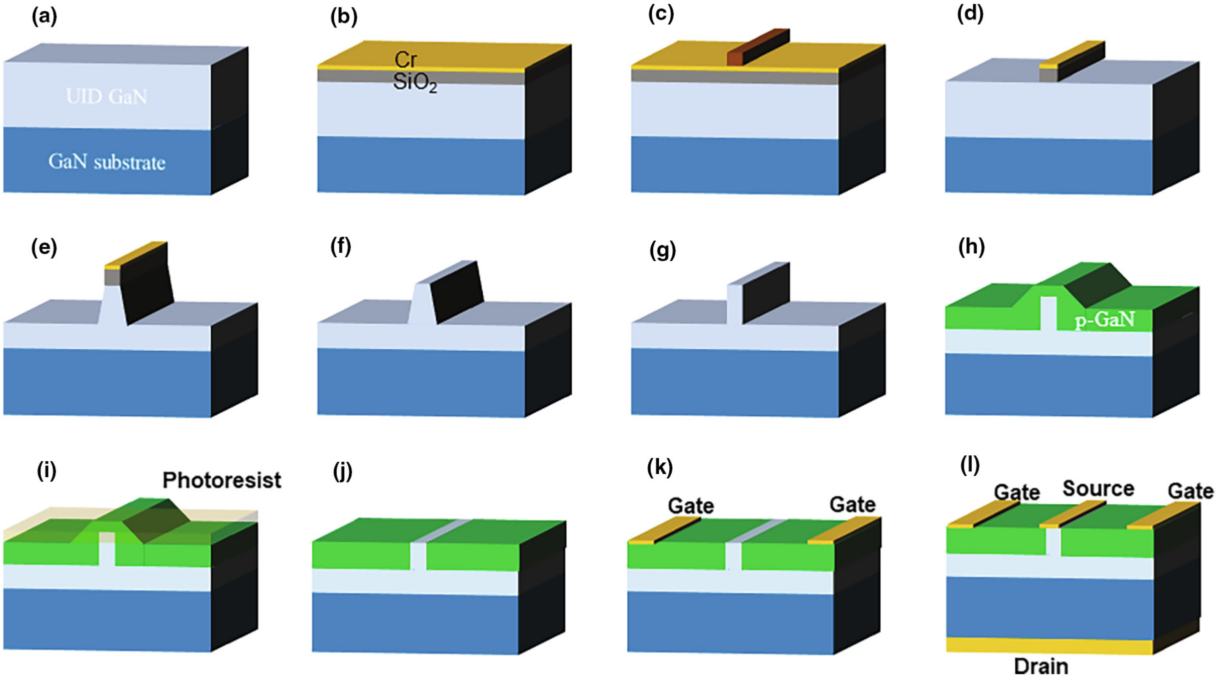

FIGURE 26

Fabrication processes of the VJFETs. (a) Starting epilayers; (b) Cr and SiO_2 hard masks; (c) e-beam lithography for fins; (d) Hard masks removal; (e) ICP etching; (f) Hard masks removal; (g) TMAH etching; (h) p-GaN regrowth; (i) Self-planarization using photoresist; (j) Top p-GaN removal; (k) Gate metal contacts deposition; (l) Source and drain metal contacts deposition. © [2020] IEEE. Reprinted with permission from Ref. [159].

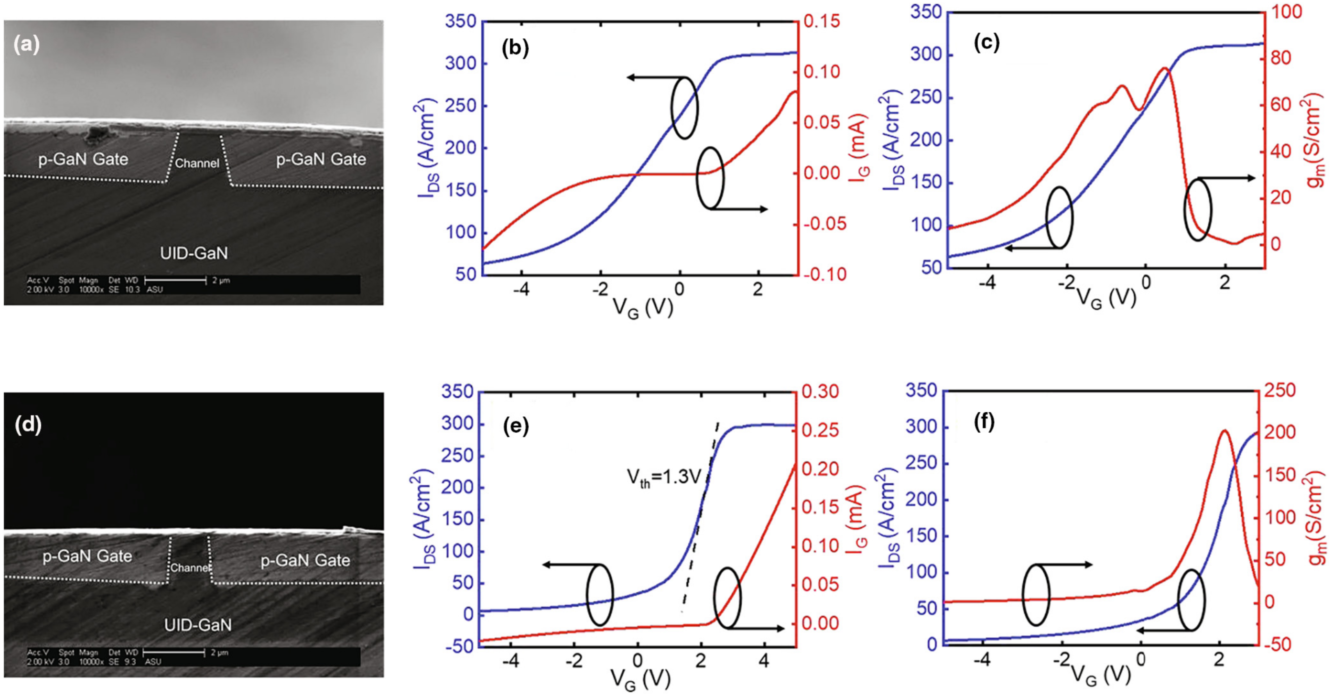

FIGURE 27

(a) Cross-sectional SEM image of the first-generation VJFETs. (b) I_D, I_G–V_G and (c) g_m of the first-generation VJFETs at V_D of 3 V. (d) Cross-sectional SEM image of the second-generation VJFETs. (e) I_D, I_G–V_G and (f) g_m of the second-generation VJFETs at V_D of 10 V. © [2020] IEEE. Reprinted with permission from Ref. [159].

ized by the total active area of the fins. In the development of normally-off VJFETs, two sets of experiments were carried out to optimize the device growth and structures. In the first-generation VJFETs, no TMAH treatment was applied prior to p-GaN gate regrowth. Fig. 27a shows a cross-sectional SEM image of the VJFETs. A slanted sidewall was clearly observed, leading to a channel region with increasing width from top to bottom. In addition, an n^+-GaN layer was employed as the source.

Please cite this article in press as: H. Fu et al., Materials Today, (2021), https://doi.org/10.1016/j.mattod.2021.04.011

Fig. 27b shows the transfer characteristics and gate leakage of the VJFETs. The device showed gate modulation. However, the device had a normally-on operation, possibly in part due to the slanted channel. In addition, the I_{on}/I_{off} ratio was ∼6, and the gate leakage was relatively large. The transconductance g_m exhibited two peaks (Fig. 27c), indicating the presence of interface charges.

Although the first-generation VJFETs have shown transistor characteristics, the relatively poor device performance may result from a combination of factors such as interfacial defects and impurities, etching damage, a slanted channel, and source-to-gate tunneling. To realize normally-off VJFETs with improved performance in the second-generation VJFETs, TMAH wet etching, and UV-ozone and HF treatments were applied prior to regrowth to remove possible etching damage, and interfacial charges and impurities. TMAH etching can also result in a more vertical sidewall aligned to *m*-plane (Fig. 27d). Furthermore, the sample did not have an n^+-GaN layer as the source to prevent forming Zener junctions between the source and the gate, which may give rise to a large gate leakage. Instead, the source region was treated with ICP etching to create donor-like surface defects to facilitate contacts. Fig. 27e shows the transfer characteristics and gate leakage of the second-generation VJFETs. A threshold voltage (V_{th}) of ∼1.3 V was obtained. At V_{GS} = 3.4 V and V_{DS} = 10 V, the drain current density reached ∼300 A/cm^2. Further increase in V_{GS} led to the forward bias of the gate-to-source junctions and the ramp-up of gate current. The I_{on}/I_{off} was improved significantly to ∼100. The gate leakage was also reduced compared with the first-generation VJFETs. The transconductance curves of the devices (Fig. 27f) showed a single peak with an excellent peak value of ∼200 S/cm^2, which is among the best values ever reported for vertical GaN VJFETs. The breakdown voltages of the devices were still relatively low (<100 V), which still need improvements. Recently, Liu et al. [160] demonstrated 1.2 kV-class Fin JFETs with avalanche capability.

Conclusions and outlook

This paper reviews materials challenges and recent progress on selective area regrowth and doping for vertical GaN power devices. By investigating the effects of trench width and depth on regrowth, lateral and basal plane growth modes were identified. Shallow trenches with an optimized width are optimal for selective area regrowth. Several materials characterization techniques were used to profile the dopant distributions at the submicron scale and to study the regrowth interface. It was found that there was nonuniform Mg distribution in a mesa or trench structure. The regrowth interface showed large amounts of impurities and charges, resulting in the formation of a p^+-n^+ tunneling junction. This may partly explain the large reverse leakage currents in regrown p-n junctions. Three novel etching technologies were employed to improve the regrowth interface. Low-power ICP dry etching significantly reduced the charge concentrations at the regrowth interface and decreased the reverse leakage currents. To reduce dry etching damage or replace ICP dry etching, PEC, ALE, and TBCl-based *in situ* and selective area etching have been developed, and relevant studies in selective area regrowth are ongoing. Based on the improved selective area regrowth, decent regrown p-n junctions and the first normally-off VJFETs were demonstrated. These results represent an important step toward the realization of selective area regrowth and doping.

Despite this encouraging progress in selective area regrowth and doping for GaN, there are still some issues that remain to be investigated and explored to facilitate the maturity of the technique. Firstly, most of the current materials characterizations are based on planar etched samples. More work is needed on the characterizations of regrown structures in trenches (especially their sidewalls), including impurity control, etching methods, post-etching treatments, and electronic structures. Electrical characterizations of the lateral p-n junctions are essential, including *I–V* and *C–V*. The current leakage through the sidewall must be suppressed for the lateral p-n junction to properly function in complicated device structures. Secondly, most selective area regrowth and doping studies are currently focused on the *c*-plane and nonpolar *m*-plane. However, ICP etching often results in a trench with a semipolar plane sidewall instead of an *m*-plane sidewall. Regrowth dynamics and materials characterizations for semipolar plane devices demand further investigation. Thirdly, although some etching techniques show promising results, how these novel etching technologies affect the performance of regrown GaN devices still requires significant research effort. It is also important to investigate how to increase the etching rate without creating more damage at the regrowth interface. Fourthly, there are currently still very few reports on regrown GaN devices, and the demonstrated devices usually have relatively simple structures. More complicated device structures such as vertical GaN JBS/MPS rectifiers, JTE, and even insulated-gate bipolar transistors (IGBTs) should be studied. Finally, the regrowth interface in the regrown devices could become a reliability concern for mass production. Therefore, it is critical to evaluate the stability of these regrown devices over an extended time period under high temperature and high voltage stress. Comprehensive failure analysis should be performed to identify the failure modes and failure mechanisms, which can be used to assist the device regrowth and design optimization.

Selective area regrowth and doping in vertical GaN power devices is a highly interdisciplinary area that requires collaborations from electrical engineers, materials, physicists, and chemists. This comprehensive and timely review can serve as a useful reference for general readers and experts in the field, and show the way to more opportunities for interdisciplinary research and exciting advances in the development of vertical GaN power electronics and systems.

Declaration of Competing Interest

The authors declare that they have no known competing financial interests or personal relationships that could have appeared to influence the work reported in this paper.

Acknowledgment

This work is supported by ARPA-E PNDIODES Program monitored by Dr. Isik C. Kizilyalli.

References

[1] S. Chowdhury, U.K. Mishra, IEEE Trans. Electron Devices 60 (2013) 3060–3066.

Please cite this article in press as: H. Fu et al., Materials Today, (2021), https://doi.org/10.1016/j.mattod.2021.04.011

[2] S. Chowdhury, et al., Semicond. Sci. Technol. 28 (2013) 074014.
[3] H. Amano et al., J. Phys. D: Appl. Phys. 51 (2018) 163001
[4] Y. Zhang, A. Dadgar, T. Palacios, J. Phys. D: Appl. Phys. 51 (2018) 273001.
[5] J.Y. Tsao et al., Adv. Electron. Mater. 4 (2018) 1600501.
[6] J. Wei et al., Jpn. J. Appl. Phys. 59 (2020) SG0801.
[7] H. Fu, K. Fu, and Y. Zhao, "Vertical GaN-on-GaN power devices", chapter in "Wide bandgap semiconductors", edited by Profs. S. J. Pearton and F. Ren, IOP Science, (2020).
[8] K.J. Chen et al., IEEE Trans. Electron Devices 64 (2017) 779–795.
[9] R. Sun et al., IEEE Access 8 (2020) 15529–15542.
[10] T. Ueda, Jpn. J. Appl. Phys. 58 (2019) SC0804.
[11] T. Oka, Jpn. J. Appl. Phys. 58 (2019) SB0805.
[12] I.C. Kizilyalli et al., IEEE Trans. Electron. Devices 62 (2015) 414–422.
[13] Y. Cao, et al., Appl. Phys. Lett. 108 (2016) 062103.
[14] H. Fu, et al., Appl. Phys. Lett. 111 (2017) 152102.
[15] S. Han, S. Yang, K. Sheng, IEEE Electron. Device Lett. 40 (2019) 1040–1043.
[16] S. Han, S. Yang, K. Sheng, IEEE Electron. Device Lett. 39 (2018) 572–575.
[17] Y. Cao, et al., Appl. Phys. Lett. 108 (2016) 112101.
[18] L. Sang et al., Appl. Phys. Lett. 111 (2017) 1221102.
[19] B. Ren, et al., Appl. Phys. Express 10 (2017) 051001.
[20] N. Tanaka, et al., Appl. Phys. Express 8 (2015) 071001.
[21] Y. Saitoh, et al., Appl. Phys. Express 3 (2010) 081001.
[22] H. Fu et al., IEEE Electron. Device Lett. 41 (2020) 127–130.
[23] I.C. Kizilyalli, T. Prunty, O. Aktas, IEEE Electron. Device Lett. 36 (2015) 1073–1075.
[24] H. Fu et al., IEEE Electron Device Lett. 38 (2017) 763–766.
[25] I.C. Kizilyalli et al., IEEE Trans. Electron Devices 60 (2013) 3067–3070.
[26] H. Fu, et al., Appl. Phys. Express 11 (2018) 111003.
[27] I.C. Kizilyalli et al., IEEE Electron. Device Lett. 35 (2014) 247–249.
[28] J. Wang, et al., Appl. Phys. Lett. 113 (2018) 023502.
[29] K. Nomoto et al., IEEE IEDM, (2015) 9.7.1-9.7.4.
[30] J. Wang, et al., IEEE IEDM, (2017) 9.6.1-9.6.4.
[31] Z. Hu et al., Appl. Phys. Lett. 107 (2015) 243501.
[32] K. Nomoto et al., IEEE Electron Device Lett. 37 (2016) 161–164.
[33] H. Fukushima S. Usami M. Ogura Y. Ando A. Tanaka M. Deki M. Kushimoto S. Nitta Y. Honda H. Amano Jpn. J. Appl. Phys. 58 2019 SCCD25
[34] H. Fukushima et al., Appl. Phys. Express 12 (2019) 026502.
[35] T. Maeda, et al., IEEE IEDM, (2018) 30.1.1-30.1.4.
[36] H. Fu et al., IEEE Electron Device Lett. 39 (2018) 1018–1021.
[37] T. Maeda et al., IEEE Electron Device Lett. 40 (2019) 941–944.
[38] H. Fu et al., Appl. Phys. Express 12 (2019) 051015.
[39] S. Usami et al., Appl. Phys. Lett. 112 (2018) 182106.
[40] B. Rackauskas et al., Appl. Phys. Lett. 112 (2018) 233501.
[41] D. Ji, B. Ercan, S. Chowdhury, Appl. Phys. Lett. 115 (2019) 073503.
[42] L. Cao, et al., Appl. Phys. Lett. 112 (2018) 262103.
[43] Y. Zhang et al., IEEE Electron Device Lett. 38 (2017) 1097–1100.
[44] Y. Zhang, et al., IEEE IEDM, (2016) 10.2.1-10.2.4.
[45] Y. Zhang, et al., Appl. Phys. Lett. 110 (2017) 193506.
[46] T. Hayashida et al., Appl. Phys. Express 10 (2017) 061003.
[47] W. Li et al., IEEE Trans. Electron Devices 64 (2017) 1635–1641.
[48] C. Gupta et al., IEEE Electron Device Lett. 38 (2017) 353–355.
[49] D. Ji, et al., IEEE IEDM, (2017) 9.4.1-9.4.4.
[50] D. Ji et al., IEEE Electron Device Lett. 39 (2018) 711–714.
[51] T. Oka et al., Appl. Phys. Express 8 (2015).
[52] T. Oka et al., Appl. Phys. Express 7 (2014).
[53] R. Li et al., IEEE Electron Device Lett. 37 (2016) 1466–1469.
[54] H. Nie et al., IEEE Electron Device Lett. 35 (2014) 939–941.
[55] D. Shibata, et al., IEEE IEDM, (2016) 10.1.1-10.1.4.
[56] D. Ji et al., IEEE Trans. Electron Devices 64 (2017) 805–808.
[57] M. Sun et al., IEEE Electron Device Lett. 38 (2017) 509–512.
[58] Y. Zhang, et al., IEEE IEDM, (2017) 9.2.1-9.2.4.
[59] B.J. Baliga, Fundamentals of Power Semiconductor Devices, Springer-Verlag, New York, 2008.
[60] B.J. Baliga, Silicon Carbide Power Devices, World Scientific, Singapore, 2005.
[61] W. Sung et al., IEEE Electron Device Lett. 32 (2011) 880–882.
[62] A.V. Bolotnikov et al., IEEE Trans. Electron Devices 57 (2010) 1930–1935.
[63] R. Ghandi et al., IEEE Trans. Electron Devices 58 (2011) 2665–2669.
[64] A. Salemi et al., IEEE Electron Device Lett. 39 (2018) 63–66.
[65] B.N. Feigelson et al., J. Cryst. Growth 350 (2012) 21–26.
[66] J.D. Greenlee et al., ECS J. Solid State Sci. Technol. 4 (2015) P382–P386.
[67] H. Sakurai et al., Appl. Phys. Lett. 115 (2019) 142104.
[68] K. Fu et al., Appl. Phys. Lett. 113 (2018) 233502.
[69] M. Monavarian et al., IEEE Electron Device Lett. 40 (2019) 387–390.
[70] S.W. King et al., J. Appl. Phys. 84 (1998) 5248.
[71] G. Koblmüller et al., J. Appl. Phys. 107 (2010) 043527.
[72] A.L. Rosa, J. Neugebauer, Phys. Rev. B 73 (2006) 205314.
[73] A. Aragon et al., Phys. Status Solidi A 217 (2020) 1900757.
[74] M. Yang et al., J. Cryst. Growth 311 (2009) 2914–2918.
[75] Z. Zheng et al., Phys. Status Solidi (a) 208 (2011) 951–954.
[76] F. Yang et al., J. Mater. Sci. Mater. Electron. 26 (2015) 9753–9758.
[77] S.R. Alugubelli et al., J. Appl. Phys. 126 (2019) 015704.
[78] H. Liu, et al., Appl. Phys. Lett. 114 (2019) 082102.
[79] P.-Y. Su et al., Appl. Phys. Lett. 117 (2020) 102110.
[80] P.-Y. Su et al., J. Appl. Phys. 128 (2020) 055301.
[81] H. Liu et al., J. Appl. Phys. 127 (2020) 195701.
[82] K. Hiramatsu et al., J. Cryst. Growth 221 (2000) 316.
[83] J. Wang et al., Semicond. Sci. Technol. 35 (2020) 125026.
[84] S. Nakamura et al., Jpn. J. Appl. Phys. 31 (2020) 1258.
[85] S.M. Myers et al., J. Appl. Phys. 89 (2001) 3195.
[86] Y. Kuwano et al., Jpn. J. Appl. Phys. 52 (2013) 08JK12.
[87] W. Li et al., Appl. Phys. Lett. 113 (2018).
[88] W. Li et al., IEEE Trans. Electron Devices 65 (2018) 2558–2564.
[89] W. Li et al., Proc. 75th Annu. Device Res. Conf. (DRC) (2017).
[90] W. S. Li, et al., Jpn. J. Appl. Phys., Part 1 58 (2019) SCCD15.
[91] Z. Hu et al., IEEE Electron Device Lett. 38 (2017) 1071–1074.
[92] S. Guha et al., Appl. Phys. Lett. 75 (1999) 463.
[93] H. Sekiguchi et al., Appl. Phys. Express 1 (2008) 124002.
[94] A. Bengoechea-Encabo et al., J. Cryst. Growth 325 (2011) 89.
[95] R. Yeluri et al., Appl. Phys. Lett. 106 (2015) 183502.
[96] K. Grabianska et al., Electronics 9 (2020) 1342.
[97] B. Raghothamachar et al., J. Cryst. Growth 544 (2020) 125709.
[98] Y. Liu et al., J. Cryst. Growth 551 (2020) 125903.
[99] M. Lee et al., CrystEngComm. 19 (2017) 2036.
[100] P. Peri, et al., J. Vac. Sci. Technol. A 38 (2020) 063402.
[101] S.C. Cruz et al., J. Cryst. Growth 311 (2009) 3817–3823.
[102] A. Chakraborty et al., J. Appl. Phys. 96 (2004) 4494.
[103] J. Wang et al., Phys. Status Solidi A 211 (2014) 2645–2649.
[104] F. Shahedipour, B.W. Wessels, Appl. Phys. Lett. 76 (2000) 3011.
[105] H. Amano et al., J. Electrochem. Soc. 137 (1990) 1639.
[106] U. Kaufmann et al., Appl. Phys. Lett. 72 (1998) 1326.
[107] J. Cazaux, J. Electron Microsc. 61 (2012) 261.
[108] J.R. Dennison, A. Sim, C.D. Thomson, IEEE Trans. Plasma Sci. 34 (2006) 2204–2218.
[109] H. Seiler, J. Appl. Phys. 54 (1983) R1.
[110] J. Goldstein, Scanning Electron Microscopy and X-ray Microanalysis, 4th ed., Springer Science, New York, 2017, p. 88.
[111] D.C. Joy, Scanning 11 (1989) 1.
[112] L. Reimer, C. Tollkamp, Scanning 3 (1980) 35.
[113] J.P. Long, V.M. Bermudez, Phys. Rev. B 66 (2002) 121308.
[114] K.M. Tracy et al., J. Appl. Phys. 94 (2003) 3163.
[115] D.D. Perovic et al., Ultramicroscopy 58 (1995) 104.
[116] I. Volotsenko, et al., J. Appl. Phys. 107 (2010) 014510.
[117] A. Shih et al., J. Appl. Phys. 82 (1997) 1860.
[118] G.F. Dionne, J. Appl. Phys. 46 (1975) 3347.
[119] A.S. Chang et al., A.C.S. Appl. Electron. Mater. 3 (2021) 704–710.
[120] P. Peri et al., J. Electron. Mater. 50 (2021) 2637–2642.
[121] H. Fu et al., IEEE Electron Device Lett. 38 (2017) 1286–1289.
[122] J. Montes et al., IEEE Trans. Nucl. Sci. 66 (2019) 91–96.
[123] H. Fu et al., IEEE Trans. Electron Devices 65 (2018) 3507–3513.
[124] T. Yang, et al., J. Semicond. 40 (2019) 012801.
[125] I. Stricklin et al., Proc. SPIE 10754 (2018) 1075402.
[126] K. Fu et al., IEEE Electron Device Lett. 40 (2019) 375–378.
[127] M.R. McCartney, D.J. Smith, Annu. Rev. Mater. Res. 37 (2007) 729.
[128] S. R. Alugubelli, et al., Appl. Phys. Lett. 115 (2019) 201602.
[129] H. Katayama-Yoshida et al., J. Phys.: Condens. Matter 13 (2001) 8901.
[130] Y. Akatsuka, et al., Appl. Phys. Express 12 (2019) 025502.
[131] E.T. Yu et al., J. Appl. Phys. 79 (1996) 2115.
[132] P.A. Rosenthal et al., J. Appl. Phys. 87 (2000) 1937.
[133] P.A. Rosenthal, Y. Taur, E.T. Yu, Appl. Phys. Lett. 81 (2002) 3993.
[134] J. Sumner, et al., J. Appl. Phys. 106 (2009) 104503.
[135] J. Sumner et al., Phys. Status Solidi B 245 (2008) 896–898.
[136] Y.J. Han et al., Jpn. J. Appl. Phys. 42 (2003) 6409.
[137] S. Tripathy et al., J. Vac. Sci. Technol. A 19 (2001) 2522.
[138] T. Narita et al., Phys. Status Solidi A 208 (2011) 1541.
[139] K. Fu et al., IEEE Electron Device Lett. 40 (2019) 1728–1731.
[140] G. W. Pickrell, et al., J. Appl. Phys. 126 (2019) 145703.

Please cite this article in press as: H. Fu et al., Materials Today, (2021), https://doi.org/10.1016/j.mattod.2021.04.011

[141] A. Aragon, et al., J. Appl. Phys. 128 (2020) 185703.
[142] Y. Lee, J.W. Dumont, S.M. George, Chem. Mater. 28 (2016) 2994–3003.
[143] Y. Lee, S.M. George, Chem. Mater. 29 (2017) 8202–8210.
[144] B. Li et al., Appl. Phys. Lett. 115 (2019) 162101.
[145] T.H. Myers et al., J. Cryst. Growth 246 (2002) 244–251.
[146] D. Fahle et al., J. Cryst. Growth 393 (2014) 89–92.
[147] J. Han et al., Appl. Phys. Lett. 71 (1997) 3114.
[148] M. Kondow, B. Shi, C.W. Tu, Jpn. J. Appl. Phys. Part 2 (38) (1999) L617.
[149] Q. An et al., J. Phys. Chem. C 119 (2015) 4095.
[150] D.R. Lide, CRC Handbook of Chemistry and Physics, CRC Press (1999–2000).
[151] D. Franke et al., J. Cryst. Growth 248 (2003) 421–425.
[152] B. Li et al., J. Cryst. Growth 534 (2020) 125492.
[153] S. Yamada et al., Appl. Phys. Express 13 (2020) 016505.
[154] S.J. Pearton et al., J. Appl. Phys. 86 (1999) 1.
[155] F.A. Khan et al., J. Vac. Sci. Technol. B 19 (2001) 2926.
[156] I.C. Kizilyalli, O. Aktas, Semicond. Sci. Technol. 30 (2015).
[157] D. Ji, S. Chowdhury, IEEE Trans. Electron Devices 62 (2015) 2571–2578.
[158] S. Kotzea et al., IEEE Trans. Electron Devices 65 (2018) 5329–5336.
[159] C. Yang et al., IEEE Trans. Electron Devices 67 (2020) 3972–3977.
[160] J. Liu et al., IEEE Trans. Electron Devices 68 (2021) 2025–2032.

Please cite this article in press as: H. Fu et al., Materials Today, (2021), https://doi.org/10.1016/j.mattod.2021.04.011